

# Journal of Materials Chemistry B

Accepted Manuscript



This is an *Accepted Manuscript*, which has been through the Royal Society of Chemistry peer review process and has been accepted for publication.

*Accepted Manuscripts* are published online shortly after acceptance, before technical editing, formatting and proof reading. Using this free service, authors can make their results available to the community, in citable form, before we publish the edited article. We will replace this *Accepted Manuscript* with the edited and formatted *Advance Article* as soon as it is available.

You can find more information about *Accepted Manuscripts* in the [Information for Authors](#).

Please note that technical editing may introduce minor changes to the text and/or graphics, which may alter content. The journal's standard [Terms & Conditions](#) and the [Ethical guidelines](#) still apply. In no event shall the Royal Society of Chemistry be held responsible for any errors or omissions in this *Accepted Manuscript* or any consequences arising from the use of any information it contains.

**Effects of zirconium and strontium on the biocorrosion of Mg-Zr-Sr alloys for  
biodegradable implant applications**

Yunfei Ding,<sup>a</sup> Yuncang Li,<sup>b\*</sup> Jixing Lin<sup>c</sup> and Cuie Wen<sup>b</sup>

<sup>a</sup>Institute for Frontier Materials, Deakin University, Geelong, Victoria 3217, Australia

<sup>b</sup>School of Aerospace, Mechanical and Manufacturing Engineering, RMIT University,  
Bundoora, Victoria 3083, Australia

<sup>c</sup>Advanced Material Research and Development Center, Zhejiang Industry & Trade  
Vocational College, Wenzhou, Zhejiang 325003, China

\*Corresponding author:

Yuncang Li

School of Aerospace, Mechanical and Manufacturing Engineering

RMIT University, Bundoora, Victoria 3083, Australia

Tel.: +613 9925 7560, Fax: +613 9925 6108

E-mail: yuncang.li@rmit.edu.au

**Abstract**

The successful applications of magnesium (Mg) alloys as biodegradable orthopedic implants are mainly restricted due to its rapid degradation rate in the physiological environment, leading to a loss of mechanical integrity. This study systematically investigated the degradation behaviors of novel Mg-Zr-Sr alloys using electrochemical techniques, hydrogen evolution, and weight loss in simulated body fluid (SBF). The microstructure and degradation behaviors of the alloys were characterized using optical microscopy, XRD, SEM, and EDX. Results indicate that Zr and Sr concentrations in Mg alloys strongly affected the degradation rate of the alloys in SBF. A high concentration of 5 wt% Zr led to an acceleration of anodic dissolution, which significantly decreased the biocorrosion resistance of the alloys and its biocompatibility. A high volume fraction of  $\text{Mg}_{17}\text{Sr}_2$  phases due to the addition of excessive Sr (over 5 wt%) resulted in enhanced galvanic effects between the Mg matrix and  $\text{Mg}_{17}\text{Sr}_2$  phases, which reduced the biocorrosion resistance. The average Sr release rate is approximately  $0.15 \text{ mg L}^{-1} \text{ day}^{-1}$ , which is much lower than the body burden and proves its good biocompatibility. A new biocorrosion model has been established to illustrate the degradation of the alloys and the formation of degradation products on the surface of the alloys. It can be concluded that the optimal concentration of Zr and Sr is less than 2 wt% for as-cast Mg-Zr-Sr alloys used as biodegradable orthopedic implants.

## 1. Introduction

Magnesium (Mg) and Mg alloys have attracted considerable attention as promising biodegradable implant materials for biomedical applications, as they possess advantages over traditional metallic materials, ceramics, and biodegradable polymers<sup>1-3</sup>. Mg and Mg alloys gradually degrade in vivo and are eventually replaced by newly grown bone tissue after implantation, which eliminates the need for further surgery to remove the implant from the human body. However, the rapid degradation rate of existing Mg alloys in an electrolytic aqueous environment, which leads to a loss of mechanical integrity before the tissue has healed sufficiently and new bone tissue has adequately regenerated, restricts their wide application<sup>4</sup>.

To overcome this challenge, alloying elements such as aluminum (Al)<sup>5-9</sup>, calcium (Ca)<sup>10-13</sup>, manganese (Mn)<sup>14-16</sup>, zinc (Zn)<sup>14, 17-19</sup>, etc. have been utilized to develop appropriate Mg alloys which are expected to improve biocorrosion resistance as well as enhancing mechanical properties for potential use in biodegradable implants. Although Al is the most widely used alloying element in commercial Mg alloys such as AE21, AZ31, and AZ91, because of its excellent grain refinement and enhancement of biocorrosion resistance, recent studies have indicated that Al shows cytotoxicity, and chronic exposure to Al can cause adverse reactions in body tissue<sup>20</sup>. Furthermore, the accumulation of Al has been suggested to be a risk for the development of Alzheimer's disease<sup>21</sup>.

Ca is a major component presenting in the form of hydroxyapatite (HA) in human bone, and has a low density of  $1.55 \text{ g cm}^{-3}$ , which makes Mg-Ca alloys lightweight materials<sup>13</sup>. The addition of Ca to Mg leads to the formation of Mg-Ca intermetallic phases. These phases are brittle, and they distribute along grain boundaries<sup>13</sup>, which deteriorates the ductility of Mg-Ca alloys<sup>13, 22</sup>. In addition, there is reduced

biocorrosion resistance of Mg-Ca alloys with high Ca concentrations due to the galvanic effects between Mg-Ca phases and the Mg matrix<sup>22</sup>. The insoluble “chalk-like” products of the degradation of Mg-Ca alloys can be problematic in the human body if large amounts are formed<sup>23</sup>.

Mn is an essential trace element in the human body for various enzymes<sup>24</sup>. However, recent studies have raised concerns about Mn toxicity such as cytotoxicity and neurotoxicity<sup>25,26</sup>. Ding et al.<sup>25</sup> investigated the cytotoxicity of Mn on sensory hair cells, auditory nerve fibers, and spiral ganglion neurons in three rats and found that Mn exhibited toxicity in sensory hair cells. It was also found that the neurotoxicity of Mn presented as an induction factor for a disease with similar properties to Parkinson’s disease<sup>26</sup>. Zn is also a trace element for optional enzymes in the human body<sup>27</sup>. However, the amount of released Zn can become overly high through the degradation of Mg alloys with high Zn concentrations<sup>28</sup>. In addition, adverse consequences of overdoses of Zn on growth, development, and health have been reported<sup>29-31</sup>. The Zn cation acts as a mediated inhibitor of neurotrophins and can even lead to cell death<sup>32</sup>, and Zn accumulation in the human body may induce embryonic motor neuron death and affect mature motor neurons<sup>32</sup>.

A good biomedical implant should possess biomechanical compatibility with natural bone, an appropriate degradation rate, and excellent or acceptable biocompatibility that makes it harmless to host tissues. To enhance biocompatibility and provide an appropriate biodegradation rate and sufficient biomechanical properties of Mg alloys used as load-bearing implants, biocompatible alloying elements such as Zr and Sr have been utilized in Mg alloys. The alloying element of Zr can improve the ductility, refine the grain size, and smooth the grain boundaries of the Mg matrix<sup>33</sup>, and enhance the biomechanical properties and corrosion resistance of Mg alloys<sup>34</sup>. Sr can

significantly improve the osteoblastic activity and bone formation in vivo<sup>35</sup>, and thus it has been used as a biocompatible alloying element of Mg alloys<sup>36,37</sup>. Considering the benefits in the biomechanical properties, biocorrosion and biocompatibility of Zr and Sr, a novel series of Mg-Zr-Sr alloys have been developed considering the various benefits of Sr and Zr in Mg alloys<sup>38</sup>. The Mg-Zr-Sr alloys showed low cytotoxicity in vitro and good biocompatibility in vivo. The addition of Sr in Mg-Zr-Sr alloys caused the formation of an Mg<sub>17</sub>Sr<sub>2</sub> intermetallic phase which is brittle and mainly located in the grain boundary zones, leading to rougher grain boundaries in the Mg matrix, and influencing the mechanical and biocorrosion properties of the Mg<sub>5</sub>Zr<sub>5</sub>Sr alloy. It was found that high levels of Zr (> 5 wt% hereafter) and Sr (> 5 wt%) accelerate the degradation rate and subsequently result in poor biocompatibility of the biodegradable Mg alloys. However, the mechanism of the effects of Zr and Sr on the biocorrosion behaviors of Mg-Zr-Sr alloys has not been well understood<sup>39</sup>.

In this study, the degradation behaviors of Mg<sub>x</sub>Zr<sub>y</sub>Sr (x=1, 2, 5; y=2, 5 wt%) alloys in simulated body fluid (SBF) were systematically investigated. The microstructure of the Mg<sub>x</sub>Zr<sub>y</sub>Sr alloys, such as the grain size and boundary, the distribution of Zr and Sr, and the intermetallic Mg<sub>17</sub>Sr<sub>2</sub> phase, was observed using optical microscopy and scanning electron microscopy (SEM) equipped for energy-dispersive X-ray spectrometry (EDX) and an element-mapping technique. The biodegradable mechanisms of the Mg-Zr-Sr alloys in SBF were investigated using hydrogen evolution, weight loss, and electrochemical measurements (polarization curves and electrochemical impedance spectra). The variations of ion concentration for Mg and Sr in SBF were measured using ICP-MS. The effects of Zr, Sr, and the intermetallic Mg<sub>17</sub>Sr<sub>2</sub> phase on the degradable properties of Mg-Zr-Sr alloys were determined. A new biocorrosion model has been established to better understand the degradation

properties of the alloys and the formation of biodegradation products on the surface of the alloys.

## 2. Materials and methods

### 2.1 Preparation of Mg alloys

Mg<sub>x</sub>Zr<sub>y</sub>Sr (x=1, 2, 5; y=2, 5, wt% hereafter) alloys were prepared by casting from melts of pure Mg, Mg-30Zr and Mg-30Sr master alloys (Hunan Rare Earth Metals and Materials Institute, China). High-purity Mg (99.98 %) was melted in a coated steel crucible heated to 700° C. Subsequently Mg-30Zr and Mg-30Sr were added to the melt in an atmosphere of high-purity argon. The melt was constantly stirred for 30 minutes and cast into cylindrical steel dies with an inner diameter of 22 mm and preheated to 250° C. The chemical compositions of the Mg alloys were determined by wavelength dispersion X-ray fluorescence (WDXRF, S4 Pioneer, Bruker, Germany). Samples with a diameter of 10 mm and thickness of 3 mm were further machined using electrical discharge machining (EDM) along the long axis of the Mg alloy ingots for microstructure characterization, phase analysis, and immersion tests.

### 2.2 Microstructure

The microstructure of the alloys was investigated using optical microscopy and scanning electron microscopy (SEM, Supra 55, Zeiss) equipped for energy-dispersive X-ray spectrometry (EDX) with an element-mapping technique. X-ray diffraction (XRD) was used to characterize the phase constituents of the Mg alloys before and after immersion tests. All samples for microstructure observation were mounted using cold epoxy resin with one side exposed, ground using 1200 grit SiC paper under running water, then mechanically polished on a Struers twin-disc RotoPol 22 fitted with a RotoForce-4 controller using a 1 μm diamond suspension with felt nap mats.

Finally, samples were ethanol-cleaned to remove any contamination and further etched with picric acid (a solution of 3.0 ml picric acid, 50 ml ethanol, 5 ml acetic acid, and 10 ml distilled water).

### 2.3 Hydrogen evolution and weight loss

Mg degradation in physiological environments generally proceeds through an electrochemical reaction with water to produce magnesium hydroxide ( $\text{Mg}(\text{OH})_2$ ) and hydrogen gas ( $\text{H}_2$ )<sup>40</sup>, so that the degradation rate of Mg alloys is related to the volume of hydrogen generated. The hydrogen evolution method is one of the reliable methods for determining the biodegradation rate of Mg alloys in physiological environments<sup>17, 38, 41</sup>. During the immersion tests, the Mg-Zr-Sr alloy specimens were put into beakers filled with SBF. A funnel was placed over the specimens to collect the hydrogen gas produced from the specimens during degradation. The hydrogen gas was collected using a burette above the inverted funnel that covered the samples<sup>42</sup>. In this study, Mg-Zr-Sr alloys were immersed in SBF with a water bath at 37 °C. The ratio of the sample surface area ( $\text{cm}^2$ ) to the volume of SBF solution (ml) was 1:300. Samples with a diameter of 10 mm and thickness of 3 mm were mounted in epoxy resin with an exposed area of  $0.785 \text{ cm}^2$  and immersed in SBF solution. The degradation rate  $P_h$  (mm per year) was determined by the hydrogen evolution rate  $V_h$  ( $\text{ml cm}^{-2}$  per day) using the equation<sup>42</sup>:

$$P_h = 2.279 V_h \quad (1)$$

After the hydrogen evolution tests, the degraded samples were quickly removed from the beakers, cleaned with distilled water, and dried. The corrosion products were removed using a  $200 \text{ g L}^{-1}$  chromic acid solution. The weight of the samples before and after the tests was measured using an analytical balance with a precision of 0.001

g. The degradation rate  $P_w$  (mm per year) was calculated from the weight loss rate  $\Delta W$  (mg cm<sup>-2</sup> per day) using the equation<sup>43</sup>:

$$P_w = 2.10 \Delta W \quad (2)$$

#### 2.4 Electrochemical measurement

Samples with a diameter of 10 mm and thickness of 3 mm were used for the electrochemical tests. All samples were connected to a copper wire and then encapsulated in cold epoxy resin with one side exposed to SBF<sup>22</sup>. The sample surface was mechanically ground with 1200 grit SiC paper, polished using a 9  $\mu$ m diamond suspension with felt nap mats, washed with acetone, ethanol, and distilled water, and dried in a cool airstream. The electrochemical measurement was carried out using a Multichannel potentiostat (VSP, Bio-logic France) equipped with Multistate software in a digital thermostat at the temperature of  $37 \pm 0.3$  °C. A three-electrode cell system with a saturated calomel electrode (SCE) as the reference electrode, a platinum electrode (15  $\times$  15  $\times$  1 mm) as the counter electrode, and the sample mounted in cold epoxy resin as the working electrode was used in this study.

In order to understand the influences of Zr and Sr additions on the degradation behaviors of Mg-Zr-Sr alloys, electrochemical impedance spectra (EIS) fitted with ZsimpWin software were measured at a frequency range from 10 mHz to 100 kHz at 10 mV in amplitude. Before the electrochemical tests, the samples were kept in SBF for 2 h to stabilize the open-circuit potential (OCP). Each specimen was kept floating at the OCP and, for each measurement of EIS, the potential was set to the actual OCP. Potentiodynamic polarization testing was conducted for each alloy after EIS measurement. The potential of the electrodes was swept at a rate of 0.5 mv s<sup>-1</sup> ranging from an initial potential of  $\pm 500$  mv versus OCP. The corrosion current density ( $i_{corr}$ ) and degradation rate were calculated using EC-lab software provided by Bio-logic.

## 2.5 Ion release and surface characterization after immersion in SBF

To investigate the degradation behavior of Mg-Zr-Sr alloys, cylinder samples with a diameter of 10 mm and thickness of 3 mm mounted with epoxy were immersed in SBF. The ion concentrations of the prime metallic elements of Mg and Sr from disk samples for different immersion time periods were analyzed using an inductively coupled plasma mass spectrometer (ICP-MS, Agilent 7700x) with an Agilent ASX 520 Auto sampler. Due to the high resistance to water, alkalis and acids of Zr, the measurement of ion concentrations of Zr were only possible in this study. Before analyses, the solutions with Mg and Sr ions were filtered through 0.22  $\mu\text{m}$  membrane filters, and then were diluted with ultra-pure water acidified with 2 %  $\text{HNO}_3$ . Ion concentrations were calculated as  $\text{mg L}^{-1}$  using corresponding regression lines (correlation factor  $\geq 0.999$ ).

The surface morphologies after immersion in SBF and polarization tests were observed by SEM. The surface of Mg-Zr-Sr alloys after immersion tests was investigated using EIS combined with Nyquist plots. The chemical compositions of the corrosion products were characterized using XRD and EDX techniques.

## 3. Results

### 3.1 Microstructure

To investigate the biodegradation behaviors of Mg-Zr-Sr alloys with different Zr and Sr concentrations, as-cast Mg<sub>1</sub>Zr<sub>2</sub>Sr, Mg<sub>1</sub>Zr<sub>5</sub>Sr, Mg<sub>2</sub>Zr<sub>2</sub>Sr, and Mg<sub>5</sub>Zr<sub>2</sub>Sr alloys were studied while as-cast Mg was used as a reference. Fig. 1 shows the microstructures of as-cast Mg<sub>1</sub>Zr<sub>2</sub>Sr, Mg<sub>1</sub>Zr<sub>5</sub>Sr, Mg<sub>2</sub>Zr<sub>2</sub>Sr, and Mg<sub>5</sub>Zr<sub>2</sub>Sr alloys. It can be seen that the grain size within each alloy was homogenous; however, the grain size decreased with an increase in Zr, as can be seen in the alloys of Mg<sub>1</sub>Zr<sub>2</sub>Sr,

Mg<sub>2</sub>Zr<sub>2</sub>Sr, and Mg<sub>5</sub>Zr<sub>2</sub>Sr (Figs. 1a, c and d). The microstructure of Mg<sub>1</sub>Zr<sub>5</sub>Sr (Fig. 1b) showed a thicker grain boundary compared to the other alloys, and the grain size decreased compared to that of Mg<sub>1</sub>Zr<sub>2</sub>Sr with the same Zr content, which indicates that the high Sr content refined the grain size of the Mg alloys but caused thick grain boundaries (Figs. 1a and b).

Fig. 2 shows the XRD patterns of the as-cast Mg-Zr-Sr alloys. The peaks of the phases, including Zr, the Mg matrix, and intermetallic Mg<sub>17</sub>Sr<sub>2</sub>, were identified for the alloys before the immersion tests. The peaks of the Mg<sub>17</sub>Sr<sub>2</sub> phases intensified with increasing Sr content (as shown in Mg<sub>1</sub>Zr<sub>5</sub>Sr), which suggests that the Sr addition to the Mg alloys led to the formation of the Mg<sub>17</sub>Sr<sub>2</sub> phases. The alloying element distributions of the Mg<sub>1</sub>Zr<sub>5</sub>Sr alloy (with the highest Sr content) and the Mg<sub>5</sub>Zr<sub>2</sub>Sr alloy (with the highest Zr content) were characterized using EDX mapping and are shown in Figs. 3 and 4, respectively. It can be seen that the grain boundaries were rich in Sr, indicating that the Mg<sub>17</sub>Sr<sub>2</sub> phases were distributed along grain boundaries. In addition to the Mg<sub>17</sub>Sr<sub>2</sub> phase, the Mg matrix and the fine distribution of Zr are also visible in the EDX mapping. Due to the higher content of Zr in Mg<sub>5</sub>Zr<sub>2</sub>Sr than in Mg<sub>1</sub>Zr<sub>5</sub>Zr, finer distributions of Zr are observed in the mapping of Mg<sub>5</sub>Zr<sub>2</sub>Sr. The fine distributions of Zr were located in the interior of the Mg matrix, with less Zr distributed on the grain boundaries. The different size and brightness of particles in the EDX mapping of Zr indicate the non-homogeneous distribution and particle size. The Mg<sub>17</sub>Sr<sub>2</sub> phase and the fine distribution of the Zr phase have different potentials to that of the Mg matrix. This potential difference may lead to galvanic effects for Mg-Zr-Sr alloys, and significantly affect the degradation behavior<sup>38, 44</sup>.

### 3.2 Degradation behaviors of Mg-Zr-Sr alloys

To investigate the effects of Zr and Sr on the degradation of the Mg alloys, the hydrogen evolution of Mg-Zr-Sr alloys in SBF against immersion time was measured and this is summarized in Fig. 5. As can be seen, Mg alloys with different Zr and Sr additions suffered different attacks from SBF in the increasing order of Mg1Zr2Sr < as-cast Mg < Mg2Zr2Sr < Mg1Zr5Sr < Mg5Zr2Sr, which suggests that Mg1Zr2Sr and Mg2Zr2Sr are relatively stable compared to Mg1Zr5Sr and Mg5Zr2Sr. The hydrogen evolution curves indicate that Mg5Zr2Sr exhibited the highest degradation rate of all Mg alloys, which may be attributable to the accelerated galvanic effects of both the single phase of Zr and the intermetallic Mg<sub>17</sub>Sr<sub>2</sub> phase. During the hydrogen evolution testing, Mg1Zr5Sr produced less hydrogen gas than Mg5Zr2Sr but more hydrogen gas in comparison to the other Mg alloys. Based on the hydrogen evolution curves, it is noted that the addition of excessive Zr and Sr to Mg reduced the biocorrosion resistance. Fig. 6 shows the weight loss rates of the Mg-Zr-Sr alloys after the immersion tests. The weight loss for Mg1Zr2Sr was 7.05 mg cm<sup>-2</sup> per day, which is 2.74 times lower than that of as-cast pure Mg (19.13 mg cm<sup>-2</sup> per day). Both the hydrogen evolution and the weight loss tests clearly indicate that Mg1Zr2Sr exhibited the lowest degradation rate among all the Mg alloys studied, while Mg1Zr5Sr and Mg5Zr2Sr showed relatively high degradation rates in SBF in comparison to other Mg-Zr-Sr alloys.

The degradation rates related to hydrogen evolution and weight loss were calculated according to Eqs. (1) and (2) and are shown in Fig. 7. It can be seen that Mg1Zr2Sr exhibited the lowest degradation rate in comparison to the other Mg alloys studied and the reference as-cast Mg. The degradation rates of the Mg-Zr-Sr alloys based on hydrogen evolution were slightly lower than or relatively close to those based on

weight loss. The difference was probably caused by the uncollected hydrogen gas bubbles that adhered to the burette walls.

In general, the cathodic polarization curve is controlled by the hydrogen evolution reaction through water reduction, whereas the anodic polarization curve represents the degradation of Mg in SBF<sup>45,46</sup>. The polarization curves of the Mg-Zr-Sr alloys after 2 h of stabilization in SBF and the results are shown in Fig. 8 and Table 1, respectively. It can be seen that the current density showed an increase with increasing Sr content from Mg1Zr2Sr to Mg1Zr5Sr. Generally, high current density in a polarization test represents a high degradation rate. Thus, among all the Mg-Zr-Sr alloys, Mg1Zr2Sr exhibited the lowest degradation rate, whereas Mg5Zr2Sr showed the most rapid degradation. It can be concluded that the addition of excessive Zr (5 %) to the Mg alloys greatly reduced the biocorrosion resistance. In particular, the addition of excessive Zr to the Mg alloys resulted in an increase in the cathodic reaction kinetics and a reduction in the anodic reaction kinetics, and therefore accelerated the anodic dissolution in the polarization tests. It should be noted that Sr played a different role than Zr in the corrosion kinetics. The OCP of the Mg matrix moved in a positive direction with increasing Sr addition from 2 % to 5 % and, therefore, the cathodic reaction preferentially occurred on the cathodic branches, which led to accelerated degradation rates in the polarization tests.

The EIS spectra for the Mg-Zr-Sr alloys and as-cast Mg measured at the corrosion potential in SBF are presented in Fig. 9. As can be seen, their responses to an applied corrosion potential were significantly different. The Nyquist spectra of Mg1Zr2Sr and cast Mg display two high and medium frequency capacitance loops, as well as one low frequency inductive loop. However, Mg1Zr5Zr, Mg2Zr2Sr, and Mg5Zr2Sr showed different degradation behaviors, and the Nyquist plots of these alloys consist

of a high to medium frequency capacitance loop and a medium to low frequency inductive loop. The inductive loop is attributable to the partially protective surface layer, and the capacitance loop is related to the  $\text{Mg}^+$  ion concentration within the broken area of the surface<sup>47</sup>. In the Bode plots of  $|Z|$  versus frequency, the impedance values of Mg-Zr-Sr alloys and as-cast Mg reduce from high frequency to low frequency, and Mg5Zr2Sr showed the lowest impedance compared to the other alloys. As for the Bode plots of phase versus frequency, wave crests are visible in the low frequency regions for all alloys and as-cast Mg, indicating the presence of inductance loops.

Although pitting occurred in all Mg-Zr-Sr alloys and as-cast Mg, the degradation behaviors in SBF of the alloys were different. In order to further clarify the degradation behaviors of the Mg-Zr-Sr alloys, the EIS spectra were analyzed based on the equivalent circuits, as shown in Fig. 10. The data were fitted using an Ec-lab equipped with ZsimpWin and the results are listed in Table 2, in which  $R_s$  represents the solution resistance, CPE1 and CPE2 are the constant phase elements in parallel with the resistive elements, and each CPE has a capacitance (designated, for example,  $C_{1,T}$  and  $C_{2,T}$ ) and an associated phase angle (designated, for example,  $n_1$  and  $n_2$ ). The CPE is generally used in place of a capacitor to compensate for the non-homogeneity of the electrochemical system.  $R_{fp}$  is the resistance of a partially protective film above a localized corrosion event or micro-galvanic event,  $R_{tp}$  is the charge transfer resistance associated with the localized pitting and micro-galvanic events, and L indicates the inductance at low frequency. Generally, the diameter of the first capacitive loop at high frequency or high to medium frequency typically represents the resistance of the surface film and its influence on the degradation behaviors of Mg-Zr-Sr alloys ( $R_{fp}$ )<sup>48</sup>. A higher  $R_{tp}$  value implies a lower degradation rate<sup>47</sup>. It can

be seen that Mg1Zr2Sr had higher  $R_{fp}$  and  $R_{tp}$  values compared to the other alloys and as-cast Mg (Table 2), indicating a better resistance to biocorrosion. The lower  $R_{tp}$  value of Mg5Zr2Sr suggests severe attack in view of the absence of an inductance loop, and the significant reduction in the diameter of the capacitance loop. In the presence of  $Cl^-$  in SBF, the surface layer of the Mg-Zr-Sr alloys was chemically reactive, and the electrode processes on the surface layer of Mg5Zr2Sr were much faster than those of the other alloys due to lower biocorrosion resistance (Fig. 9b). This is the reason that the inductive loop of Mg5Zr2Sr was in a range from medium to low frequency, whereas the inductive loops at low frequency indicated breaks in the surface film and so only partial protection for the alloys.

### 3.3 Ion release and degradation morphologies of Mg alloys in SBF

The ion concentrations of Mg and Sr for Mg-Zr-Sr alloy samples with various immersion time in SBF are presented in Fig. 11 (the Sr concentration in the original SBF was deducted). ICP-MS analysis demonstrated that the variations of Mg and Sr ion concentrations in SBF depended on the immersion time and the chemical composition of Mg alloys. The ion concentration of Mg and Sr increased gradually with the prolonged immersion time in SBF. However, due to the relatively lower content of Sr in Mg-Zr-Sr alloys, the ion concentration of Sr in SBF was significantly lower than that of Mg. After immersion for 2 h, the Mg ion concentration from Mg1Zr2Sr was similar to that of Mg2Zr2Sr; whilst Mg5Zr2Sr released the highest concentration of Mg ions into SBF among all the Mg-Zr-Sr alloys. It is noted that the Mg ion concentration from Mg5Zr2Sr was 2.6 times higher than that of Mg1Zr2Sr after immersion in SBF for 48 h, which indicates a high degradation rate of Mg5Zr2Sr in SBF. Regarding the Sr ion concentration, Mg1Zr2Sr showed the lowest ion release among all the Mg-Zr-Sr alloys. At the early stage of immersion in SBF (within 6 h),

the Sr ion release from Mg<sub>5</sub>Zr<sub>2</sub>Sr was slightly higher than that of Mg<sub>1</sub>Zr<sub>5</sub>Sr. However, after immersion for 24 h, the Sr ion release in SBF for Mg<sub>1</sub>Zr<sub>5</sub>Sr reached a stable state, whilst Mg<sub>5</sub>Zr<sub>2</sub>Sr released a higher concentration of Sr ions into SBF after immersion for 48 h. The results of ion concentrations are consistent with the degradation rate of the Mg based alloy calculated from hydrogen evolution and electrochemical measurements.

Fig. 12 shows the morphologies of the Mg-Zr-Sr alloys after the polarization tests. As can be seen, some sites of the four alloys were degraded on account of the constant polarization. The surface of Mg<sub>1</sub>Zr<sub>2</sub>Sr was relatively intact with much less damage compared with the other Mg-Zr-Sr alloys, while severely corroded sites were observed for Mg<sub>5</sub>Zr<sub>2</sub>Sr (Fig. 12d), with some regions of its surface dissolved in SBF and the remainder of the surface exhibiting a loosened structure. The EDX analysis on the Mg<sub>5</sub>Zr<sub>2</sub>Sr (indicated by the arrow in Fig. 12d) showed that the peaks of oxygen and magnesium are relatively higher than other elements. The morphologies of the degraded surfaces show that the depth of corroded sites increased in the order of Mg<sub>1</sub>Zr<sub>2</sub>Sr < Mg<sub>2</sub>Zr<sub>2</sub>Sr < Mg<sub>1</sub>Zr<sub>5</sub>Sr < Mg<sub>5</sub>Zr<sub>2</sub>Sr, which indicates that Mg<sub>1</sub>Zr<sub>2</sub>Sr had the best biocorrosion resistance in SBF while Mg<sub>5</sub>Zr<sub>2</sub>Sr suffered the severest degradation.

The morphologies of the biodegraded Mg-Zr-Sr alloys after immersion in SBF for 6 h are shown in Fig. 13. It can be seen that the surface of Mg<sub>1</sub>Zr<sub>2</sub>Sr was covered with a thin degradation product and the grinding scratches were still visible, suggesting that Mg<sub>1</sub>Zr<sub>2</sub>Sr suffered a slight attack after immersion in SBF for 6 h (Fig. 13a). In the case of Mg<sub>1</sub>Zr<sub>5</sub>Sr, peeling-off occurred due to the dehydration of the surface after having been taken out of SBF and dried in cool air. However, it was still covered with an integrated surface film. The EDX investigation on spot 1 of Mg<sub>1</sub>Zr<sub>5</sub>Sr shows that

the degradation product was composed of oxygen, sodium, magnesium, strontium, phosphorus, chloride, and calcium (the carbon was from the carbon coating) (Fig. 13e). The high intensities of phosphorus, as shown in Fig. 13e, indicate that the degradation product was rich in phosphorus, oxygen, magnesium, and calcium. Mg<sub>2</sub>Zr<sub>2</sub>Sr (Fig. 13c) exhibited fewer cracks compared with Mg<sub>1</sub>Zr<sub>5</sub>Sr. The grinding scratches of Mg<sub>2</sub>Zr<sub>2</sub>Sr were still visible, and the surface showed slighter corrosion, although there were traces of peeling-off in comparison to Mg<sub>1</sub>Zr<sub>5</sub>Sr. Mg<sub>5</sub>Zr<sub>2</sub>Sr (Fig. 13d) exhibited severe corrosion and loss of surface integrity. The EDX investigation on spot 2 of Mg<sub>5</sub>Zr<sub>2</sub>Sr (Fig. 13f) shows that the peaks of phosphorus and calcium were significantly lower than those of spot 1 of Mg<sub>1</sub>Zr<sub>5</sub>Sr, suggesting different chemical compositions of the degradation products on Mg<sub>1</sub>Zr<sub>5</sub>Sr and Mg<sub>5</sub>Zr<sub>2</sub>Sr.

Fig. 14 shows the surface morphologies of the Mg-Zr-Sr alloys after 24 h of immersion in SBF. As can be seen from Fig. 14a, Mg<sub>1</sub>Zr<sub>2</sub>Sr maintained surface integrity even after 24 h of immersion in SBF. However, a peeled-off surface was observed from the highly magnified SEM image due to dehydration. The hardly visible grinding scratches indicate a stabler degradation product layer formed on the surface compared with that of 6 h immersion in SBF (Fig. 13a). In the case of Mg<sub>2</sub>Zr<sub>2</sub>Sr, many cracks divided the surface into a network structure (Fig. 14c). The SEM image at high magnification of Mg<sub>2</sub>Zr<sub>2</sub>Sr reveals that the degradation product layer on the surface had features with micro-pores, and acted as a membrane that temporarily isolated the alloy from attack by SBF. However, SBF can penetrate the micro-pores and penetrate this membrane, leading to further deterioration of the Mg substrate under the degradation product layer. Owing to the galvanic effects of Mg<sub>17</sub>Sr<sub>2</sub>, Mg<sub>1</sub>Zr<sub>5</sub>Sr showed non-uniform degradation, which was evidenced by the different thicknesses of the degradation product layer on the surface (Fig. 14b).

Mg5Zr2Sr showed the fastest degradation rate among the Mg-Zr-Sr alloys. Some regions on the surface of Mg5Zr2Sr were disintegrated into fragments. Several very large degraded holes appeared on the surface, as shown in the highly magnified SEM image (Fig. 14d). From comparison with the morphologies after polarization tests and the 6 h and 24 h degraded surfaces in SBF, it can be concluded that Mg1Zr2Sr with its degradation product layer showed the strongest biocorrosion resistance, which is consistent with the results of the hydrogen evolution, weight loss, and polarization tests, and EIS.

Fig. 15 shows the XRD patterns of the surface layers with degradation products after 24 h of immersion in SBF. It can be seen that the degradation products on the surfaces of the Mg-Zr-Sr alloys mainly contained Mg(OH)<sub>2</sub> and HA. Specifically, the intensities of Mg(OH)<sub>2</sub> and HA in Mg1Zr2Sr were higher than those of the other alloys, suggesting more effective protection provided by its degradation products.

## 4. Discussion

### 4.1 Effects of Zr on the degradation of Mg-Zr-Sr alloys

There is broad agreement that the degradation behavior of Mg alloys is significantly influenced by the grain size, grain boundary, and phase distribution<sup>46,49</sup>. The alloying element Zr has a relatively low solid solubility in an Mg matrix, and a peritectic reaction which might be the reason of grain refinement occurs between Mg and Zr when the Zr concentration exceeds about 0.58 % according to the Mg-Zr phase diagram<sup>50</sup>. Besides that, the undissolved Zr particles during solidification also act as the powerful nucleation that restrain the grain growth<sup>33, 49</sup>. The dissolved and undissolved Zr particles in Mg matrix have great effects on the biocorrosion resistance of Mg alloys<sup>17,51</sup>. Song et al.<sup>52</sup> found that the enrichment of Zr in the grain

center resulted in improvement in the corrosion resistance of this zone. However, the addition of excessive Zr to Mg (5 % in this study) led to accelerated degradation due to the galvanic effects between unalloyed Zr and the Mg matrix<sup>52</sup>. Zhou et al.<sup>51</sup> investigated the effect of Zr addition on the degradation of Mg-Ca alloys and found that the degradation rate increased significantly with an increase in Zr content in Mg-Zr-Ca alloys. Ben-Hamu et al.<sup>53</sup> reported that some sites of Mg alloys with more homogeneously distributed fine Zr particles in the Mg matrix showed a relatively lower degradation rate compared with an Mg matrix with non-homogeneously distributed Zr particles. These findings demonstrated that there is an optimal Zr concentration in Mg alloys, and the degradation rate of Mg-Zr-based alloys depends on the Zr concentration and its distribution.

The effects of Zr on degradation are clearly illustrated by the polarization curves in this study (Fig. 8). It has been found that the current density  $i_{corr}$  increased constantly with the increasing addition of Zr; this can be seen through inspection of the polarization branches in Fig. 8. The polarization curves reveal a decreased cathodic reaction with the increasing addition of Zr. Furthermore, Zr addition also significantly boosted the anodic reaction. The increase in anodic reaction rate led to an increase in current density  $i_{corr}$  although there was a slight reduction in cathodic reaction with Zr addition. It was demonstrated that the boosted anodic reaction depended on the Zr particles. The unalloyed Zr particles with the size 0.5 ~ 4.1  $\mu\text{m}$ , indicated in the EDX mapping of Mg5Zr2Sr and Mg1Zr5Sr (Figs. 3 and 4), exhibited non-homogeneous distribution in the Mg matrix, and this was the reason for the acceleration in the degradation rates of the Mg alloys<sup>41</sup>. The non-homogeneous unalloyed Zr particles had a strong correlation with the boosted anodic reaction. The surface of the Mg-Zr-Sr alloys was covered by a degradation product layer with many micro-pores, as shown

in Figs. 13 and 14. Non-homogeneously distributed Zr particles in the Mg matrix exhibited irregular sizes and configurations, which resulted in defects surrounding the Zr particles. These defects are weak links once immersed in SBF. The Mg matrix surrounding the Zr particles preferentially degrades, contributing to the galvanic effects between Zr and the Mg matrix and therefore reducing the biocorrosion resistance of the alloys. With prolonged immersion time, Zr particles may fall off the surface, resulting in more defects on the surface and leading to breakages in the degradation product layer. This process causes the occurrence of pitting.

#### 4.2 Effects of Sr on the degradation of Mg-Zr-Sr alloys

The investigation of degradation rates according to hydrogen evolution, weight loss, and polarization tests, and degradation morphologies in this study has revealed that the result with respect to the optimal amount of Sr content in Mg alloys is  $\leq 2\%$ . Gu et al.<sup>44</sup> found that binary Mg-Sr alloys with 2% Sr addition showed the best biocorrosion resistance compared with other alloys with higher Sr concentrations. They believed the improvement in the biocorrosion resistance of the Mg<sub>2</sub>Sr alloy was caused by the reduced micro-shrinkage porosity and the reduced grain size caused by Sr addition, which thus inhibited the negative effects of micro-pores on the biocorrosion resistance of the Mg alloy. Recent studies of the degradation of Mg-Sr alloys have shown broad agreement that the degradation behavior is associated with the volume fraction and distribution of the intermetallic Mg<sub>17</sub>Sr<sub>2</sub> phase<sup>38, 44</sup>. Due to the low Sr concentration in Mg alloys, the volume fraction of the Mg<sub>17</sub>Sr<sub>2</sub> phase in the Mg-Zr-Sr alloys cannot be characterized precisely. However, its volume fractions and its size in the four alloys can be easily compared based on the microstructure, indicated in Figs. 1, 3 and 4. The needle-shaped Mg<sub>17</sub>Sr<sub>2</sub> phases exhibited a netlike

distribution that was continuous, and the volume fractions increased significantly with increasing Sr addition from 2 % in Mg1Zr2Sr to 5 % in Mg1Zr5Sr. The Mg1Zr5Sr alloy exhibited the highest volume fraction of the Mg<sub>17</sub>Sr<sub>2</sub> phase distributed along the largest grain boundary zones and had the highest degradation rate compared to that of the Mg1Zr2Sr alloy.

Gu et al.<sup>44</sup> studied the degradation behaviors of binary Mg-xSr (x=1, 2, 3, 4) alloys and found that the degradation rates of Mg-xSr alloys with Sr content above 2 % increased greatly. They believed that Mg<sub>17</sub>Sr<sub>2</sub> phases are more inert than that of the Mg matrix. The Mg matrix and Mg<sub>17</sub>Sr<sub>2</sub> phases have different electrochemical potentials when exposed to aqueous environments, resulting in galvanic effects between the Mg<sub>17</sub>Sr<sub>2</sub> phase and the Mg matrix. The experimental results in this study indicate that Sr addition slightly decreased the grain size and was associated with the formation of Mg<sub>17</sub>Sr<sub>2</sub>, which strongly affected the corrosion behaviors of the Mg alloys. In the alloys with the same Zr concentration (Mg1Zr2Sr and Mg1Zr5Sr), the Mg1Zr5Sr, with more Sr, exhibited higher current density and thicker boundaries. The reduced biocorrosion resistance can be ascribed to the large grain boundary zones where more and finer Mg<sub>17</sub>Sr<sub>2</sub> resided, which enhanced the galvanic effects between the Mg<sub>17</sub>Sr<sub>2</sub> phase and the Mg matrix. This enhanced galvanic effect can be seen from the increasing corrosion potential of Mg1Zr5Sr. The polarization curves indicate that Sr addition from 2 % in Mg1Zr2Sr to 5 % in Mg1Zr5Sr resulted in an increase in the corrosion potential  $E_{corr}$  by an amount of 279 mV. This indicates that Sr is more thermodynamically stable than the Mg matrix, therefore increasing the corrosion potential of Mg1Zr5Sr. The polarization curves also reveal that the effects of Sr addition on the degradation behavior showed in the enhanced rate of the cathodic reaction and the retarded rate of the anodic reaction, which is in accordance with the

results of Gu et al.<sup>44</sup> but deviates from the results of Bornapour et al.<sup>54</sup>. In the case of the anodic branch of the polarization curves, Mg1Zr5Sr exhibited an inhibition in the degradation rate compared with Mg1Zr2Sr, which can be linked to the higher volume fraction of the Mg<sub>17</sub>Sr<sub>2</sub> phase in this alloy. However, the retardation in the anodic reaction was not great enough to counteract the increase in the cathodic reaction, and finally resulted in an increase in current density.

#### 4.3 Effects of surface layer on the degradation behavior of Mg-Zr-Sr alloys

The degradation of Mg alloys in aqueous environments mainly proceeds by a reaction with water to product magnesium hydroxide and hydrogen gas<sup>46</sup>. Zhu et al.<sup>55</sup> studied the formation of magnesium hydroxide on the surface of AZ31 in Hank's solution for 31 days and found that, at the early stage, a Mg(OH)<sub>2</sub> layer gradually formed on the alloy and led to a decrease in the degradation rate. However, this partial protection was reduced with an increase in immersion time because the thickness of the Mg(OH)<sub>2</sub> layer decreased due to attack by Cl<sup>-</sup>. Brar et al.<sup>56</sup> found that a Mg(OH)<sub>2</sub> layer was deposited on Mg-Sr alloys, and acted as a barrier film, therefore reducing the degradation rate of the Mg alloys.

In this study, EDX investigation of the degradation product layer of the Mg5Zr2Sr alloy after 6 h of immersion in SBF (Fig. 13f) showed it contained calcium, oxygen, sodium, magnesium, strontium, and phosphate. In contrast, there were only peaks for oxygen, magnesium, and chloride with Mg5Zr2Sr after immersion in SBF for 24 h (Fig. 14d). The difference in the peaks indicates the dissolution of Mg(OH)<sub>2</sub> in SBF. In addition, the XRD patterns (Fig. 15) of the Mg-Zr-Sr alloys after immersion in SBF for 24 h also reveal that Mg5Zr2Sr had the lowest intensity of Mg(OH)<sub>2</sub> compared with the other alloys. These findings imply that Mg(OH)<sub>2</sub> on the surface of Mg-Zr-Sr alloys dissolves gradually, and it only provides partial protection for Mg-

Zr-Sr alloys in SBF. It has been reported that if the medium contains any chlorides with concentrations above  $30 \text{ mmol L}^{-1}$ , the hydroxide will dissolve gradually and convert to  $\text{MgCl}_2$ <sup>57</sup>. As for the SBF in this study, the chloride content was approximately  $150 \text{ mmol L}^{-1}$ , and therefore the  $\text{Mg(OH)}_2$  on the surface was damaged gradually. Moreover, the porous structure of  $\text{Mg(OH)}_2$  as shown in Fig. 14 deteriorated rapidly because  $\text{Cl}^-$  penetrated the porous film and further attached itself to the interior Mg substrate.

It has been demonstrated that the addition of excessive Sr to Mg alloys reduces biocorrosion resistance<sup>38</sup>. However, Gu et al. revealed that Mg2Sr alloys still possess better biocorrosion resistance than pure Mg<sup>44</sup>. Brar et al. found that an Sr-substituted HA layer was observed on an Mg-Sr alloy during biocorrosion in SBF, and this layer improved the biocorrosion resistance and retarded further degradation<sup>56</sup>. Nam et al.<sup>58</sup> also found that the addition of Sr to a base material of Mg5Al had a significant effect on the grain boundaries, corrosion resistance, and surface film, and contributed to the formation of a hydroxide protective film on the Mg alloy. These findings demonstrated that Sr addition promotes the formation of an oxide layer, which leads to further protection<sup>54</sup>. Although Sr can provide these benefits to Mg alloys, the addition of excessive Sr may cause an increase in degradation due to the formation of the intermetallic phase  $\text{Mg}_{17}\text{Sr}_2$ . The oxide film around the  $\text{Mg}_{17}\text{Sr}_2$  phase is highly active because of the presence of more defects in those areas<sup>59</sup>. Addition of excessive Sr results in an increase in the volume fraction of  $\text{Mg}_{17}\text{Sr}_2$ , thus leading to the formation of more active sites around the oxide films. Generally, oxide films remain intact and maintain their integrity without interference from other phases. However, due to the presence of the  $\text{Mg}_{17}\text{Sr}_2$  phase in the Mg-Zr-Sr alloys, in particular for

Mg1Zr5Sr with a high Sr content of 5 %, the protection of the oxide film could be weakened.

Recent studies<sup>11, 38, 54, 56</sup> have indicated that there are optimal concentrations for Zr and Sr in Mg alloys. The addition of Zr in Mg alloys should be less than 2 % as further Zr addition results in more defects on the surface and boosts the anodic reaction. As for Sr addition in Mg alloys, this should not be higher than 2 %. The addition of excessive Sr leads to accelerated galvanic effects and discontinuity of the protective oxide film, which reduces the biocorrosion resistance of Mg-Zr-Sr alloys.

#### 4.4 Biocompatibilities of Zr and Sr

The biocompatibility of Mg alloy implant is influenced by the alloying elements because Mg alloy implants would directly come in contact with the host tissues inside the human body after implantation. Therefore, it is essential to understand the biocompatibility of the alloying elements of Zr and Sr.

The entry of Zr into the human body is related to the mode of exposure and the concentration in the surrounding environment. Zr behaves like an essential trace metal in nature, and it exists in soil, marine sediments, sea water and even the human body contains about 300 mg Zr<sup>60</sup>. In order to investigate the toxicokinetics and metabolism of Zr, Schroeder et al. fed 54 male and 54 female mice using drinking water with 5 mg L<sup>-1</sup> Zr(SO<sub>4</sub>)<sub>2</sub> from weaning until natural death, and they found that Zr existed in organs such as liver (10 µg L<sup>-1</sup>), kidneys (33 µg L<sup>-1</sup>) and spleen (64 µg L<sup>-1</sup>), and no notable toxicity was observed during the tests<sup>61</sup>. The good biocompatibility of Zr as alloying element in Mg was supported by a number of studies<sup>11, 62-67</sup>, in which Zr was selected as an alloying element in Mg alloys for bio-medical applications. Clayton et al<sup>68</sup> investigated the acute toxicity of various Zr compounds which were injected or fed to rats, and found that the LD<sub>50</sub> of Zr compounds was in the range of 400-10000

mg L<sup>-1</sup>, depending on the dosage and chemical composition applied on the hosts. Dolly et al.<sup>69</sup> reported that the addition of excessive Zr as high as 5 wt% to Mg alloys deteriorated the biocompatibility of Mg alloys. In their study, pure Zr was added to Mg-Sr alloys in the range of 1-5 wt%. After immersing the Mg-Zr-Sr alloy samples in SBF for 48 h, no deposits nor particles could be found in SBF for Mg1Zr2Sr, whereas a large amount of corrosion products deposited at the bottom of SBF for Mg5Zr2Sr, indicating a lower corrosion resistance of Mg alloys with excessive Zr. Li et al.<sup>38</sup> investigated the in vivo biocompatibility of Mg-(1-5)Zr-(1-5)Sr alloys, and found that Mg alloys with 5 wt% Zr addition exhibited less new bone formation, destructive mineralization and poor bonding between the Mg alloy implant and the newly formed bone, compared to Mg1Zr2Sr.

It has been reported that Sr can reanimate bone cells and inhibit bone resorption as a postmenopausal osteoporosis therapeutic agent<sup>70,71</sup>. Sr is very similar to calcium in its roles for the human body<sup>70</sup>. On account of these benefits, Sr has been used in Mg alloys for biomedical applications. Gu et al.<sup>44</sup> investigated the biocompatibility of binary Mg-Sr alloys in vitro and in vivo, and they found that Mg alloy with 2 % Sr addition exhibited enhanced bone mineralization without any destructive effect. Bornapour et al.<sup>37,54</sup> showed that Sr promotes the formation of Sr-HA layer on the Mg-Sr alloy implant after implantation into a rabbit. This Sr-HA layer significantly improves the cell growth at the interface between the Mg-Sr alloy and the degradation product. Although these studies indicated that Sr is beneficial to the biocompatibility of Mg alloys, it is still challenging to fully understand the accurate effects of Sr in the human body. After implantation, Sr inevitably converts to Sr ions and comes into the organs. Therefore, the absorption or tissue levels of Sr after implantation should not be a burden to the body. Tanaka et al.<sup>72</sup> investigated the skeletal burden of stable Sr in

Japanese adult males and found that the average Sr in skeletal is approximately 440 mg compared with 850 mg Ca. It was reported that a figure of 320 mg Sr exists in an adult weighting 70 kg ( $4.57 \text{ mg kg}^{-1}$ )<sup>73</sup>, and Sr mainly distributes in the bones and teeth of the human body ( $115\text{-}138 \text{ mg kg}^{-1}$  in average)<sup>74</sup>. In the current study, ICP-MS results showed that the average Sr release rate is approximately  $0.15 \text{ mg L}^{-1} \text{ day}^{-1}$  which is much lower than that of the body burden.

#### 4.5 Biodegradation of Mg alloys in vitro and in vivo

It is well known that the degradation behavior of Mg alloy is always related to its surrounding environment. After implantation of Mg alloy into the body, it would be exposed to aqueous environment which consists of protein, blood, and other organic and inorganic substances. As a result, Mg alloy implanted in different parts of the body may suffer various attacks from the aqueous environment of the human body<sup>75</sup>. In addition, the pH value of the interior of the human body which can significantly affect the degradation of Mg alloy implants varies from 2.0-8.0 depending on the location of the human body<sup>76, 77</sup>. Any irritation on the human body might change the pH value and thus induce the variation of degradation rate even in the same location of the human body. This change in the interior environment leads to the disparity in the degradation rate between in vitro and in vivo. Consequently, experiments on Mg alloys were principally conducted in vitro using various methods such as electrochemical measurements, hemolysis testing etc., in SBF for evaluation of degradation behavior and biocompatibility in order to minimize the disparity and provide the distinctive reference for the design of Mg alloys.

In this study, polarization, EIS, hydrogen evolution and ion release measured by using ICP-MS have been used to characterize the Mg-Zr-Sr alloys. The results indicate that Mg1ZrSr exhibited the best corrosion resistance to SBF. However, the degradation

rate derived from the hydrogen evolution was higher than that of the EIS (as indicated in Table 1). This difference in the degradation rate was caused by the rapid changes in the interface between the Mg alloy and SBF, which makes low frequency measurements difficult. It should be noted that EIS cannot be used to reveal the effects of the microstructural features such as grain size and intermetallic phase on the corrosion potential<sup>78</sup>. Furthermore, unlike the hydrogen evolution, EIS only provides the changes of Mg alloys in a short time (2 h in this study), and the surface of Mg alloys in short time may not change significantly even after 2 h stabilization, which led to a lower degradation rate of Mg alloys measured by EIS, compared with the results measured by hydrogen evolution.

#### 4.6 Biocorrosion propagation of Mg-Zr-Sr alloys in SBF

A schematic model can be established for a better understanding of the biocorrosion propagation of Mg-Zr-Sr alloys in SBF, as shown in Fig. 16. After immersion of an Mg alloy sample in SBF, an electrochemical reaction proceeds on its surface, based on three reactions<sup>46</sup>:

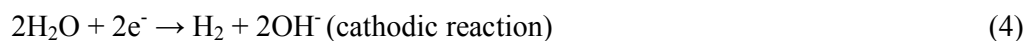


Fig. 16a illustrates the initial degradation of an Mg alloy sample exposed to SBF. The reaction in Eq. 3 mainly occurs on the exposed regions of the Mg matrix, which is directly oxidized to  $\text{Mg}^{2+}$ . The degradation of the Mg matrix is associated with the  $\text{Mg}_{17}\text{Sr}_2$  phase, as the degradation rate increases with the increasing volume fraction of  $\text{Mg}_{17}\text{Sr}_2$  due to enhanced galvanic effects. As for Mg-Zr-Sr alloys with high Zr and

Sr additions, defects on the surface allow for greater exposure to SBF and the resulting galvanic effects accelerate the degradation of the Mg matrix.

With increasing concentrations of  $Mg^{2+}$  (Eq. 3) and pH values (Eq. 4) surrounding the surface of the sample, an  $Mg(OH)_2$  film (Eq. 5) gradually forms, as shown in Fig. 16b. Thus, the degradation of the Mg alloy sample is retarded due to the presence of the protective layer of  $Mg(OH)_2$ . However, this film itself contains many micro-pores, resulting in only partial protection for Mg-Zr-Sr alloys (Fig. 14). Moreover, the film is further damaged because of corrosion, hence losing its integrity because of the non-homogeneously distributed Zr particles on the surface and the active phase of  $Mg_{17}Sr_2$ . Due to the relatively high chloride concentration in SBF, the  $Mg(OH)_2$  film in a  $Cl^-$  rich area is converted to  $Mg^{2+}$ . In addition,  $Cl^-$  penetrates the porous structural surface and further deteriorates the interior Mg matrix beneath the film, reducing the adhesion of the partially protective  $Mg(OH)_2$  film to the interior Mg matrix. The  $Mg(OH)_2$  film in some regions peels off the surface, leading to accelerated degradation (Fig. 16c). Meanwhile,  $Cl^-$  further deteriorates the sites closed to the non-homogeneous Zr particles with irregular configuration, and the Mg matrix around the  $Mg_{17}Sr_2$  phase preferentially degrades, due to the micro-galvanic effects between the  $Mg_{17}Sr_2$  phase and the Mg matrix.

Even though the Mg matrix is corroded constantly in SBF, some regions are still covered by the newly formed  $Mg(OH)_2$  film. The  $Mg^{2+}$  at the interface of the Mg matrix and SBF could pass through the porous film to form new  $Mg(OH)_2$  on the exterior surface. The constant degradation of the Mg matrix results in alkalization in the regions with fast degradation. In particular, the  $OH^-$  concentration near the substrate surface increases, and this provides nucleation sites for HA<sup>79</sup>. The undissolved  $Mg(OH)_2$  film and the newly formed  $Mg(OH)_2$  film are expected to be

the “breeding ground” for HA nucleation through consuming the  $\text{Ca}^{2+}$  and  $\text{P}^{5+}$  in the SBF (Fig. 16d).

In some regions of the Mg sample surface, the dissolution and formation of  $\text{Mg}(\text{OH})_2$  cannot reach a “dynamic equilibrium” with an uniform distribution of  $\text{Mg}(\text{OH})_2$  on the surface of the Mg-Zr-Sr alloy. Some active regions produce more  $\text{Mg}^{2+}$ , which attracts a high concentration of  $\text{Cl}^-$  in these regions. The accumulated chloride could severely attack the regions with less protection, along with the galvanic effects. Consequently, some degraded residues escape from the matrix (Fig. 16e), producing local pits in the Mg matrix, as shown in Fig. 14d. After that, the newly formed pitting might lead to more  $\text{Mg}_{17}\text{Sr}_2$  phase exposed to SBF, which further enhances the galvanic effects between the  $\text{Mg}_{17}\text{Sr}_2$  phase and the Mg matrix. Meantime, the newly exposed non-homogeneous Zr particles in the interior of Mg matrix might lead to more “defects” which attracts more attacks from  $\text{Cl}^-$  in SBF. With the deterioration of layer by layer, the Mg alloys dissolved completely.

## 5. Conclusions

In this study, the degradation behaviors of Mg-Zr-Sr alloys were systematically studied using electrochemical techniques, hydrogen evolution, and weight loss in simulated body fluid (SBF), and the optimal concentrations of Zr and Sr were established. Conclusions are as follows:

1. The Mg-Zr-Sr alloys contained fine Zr particles, an Mg matrix and an  $\text{Mg}_{17}\text{Sr}_2$  phase. The fine Zr particles were mainly distributed in the Mg matrix, which led to refined grain sizes of the Mg-Zr-Sr alloys. However, more defects on the surface

formed with the addition of excessive Zr particles and that reduced the biocorrosion resistance.

2. Compared to as-cast pure Mg, Sr addition refined the grain sizes of the Mg-Zr-Sr alloys, but it also led to the formation of an  $\text{Mg}_{17}\text{Sr}_2$  phase. The degradation rates of the Mg-Zr-Sr alloys accelerated with the addition of excessive Sr ( $>2\%$ ) due to the enhanced galvanic effects between the  $\text{Mg}_{17}\text{Sr}_2$  phase and the Mg matrix.

3. The addition of excessive Zr ( $\geq 5\text{ wt}\%$ ) to Mg alloys is a concern of biocompatibility in alloying of Mg, which would significantly deteriorate the tissue healing, reduce mineralization and lead to poor bonding. The average Sr release rate is approximately  $0.15\text{ mg L}^{-1}\text{ d}^{-1}$  which is much lower than the body burden.

3. Surface characterization reveals that an  $\text{Mg}(\text{OH})_2$  film with a porous structure formed on the surface of Mg-Zr-Sr alloys containing high Sr levels. The porous structural  $\text{Mg}(\text{OH})_2$  allowed the penetration of chloride into the interior Mg matrix, speeding up the corrosion of the Mg alloys.

4. The  $\text{Mg}_1\text{Zr}_2\text{Sr}$  alloy exhibited a degradation rate 2.74 times slower than that of pure Mg, which makes it a promising biodegradable implant material.

## References

1. F. Witte, H. Ulrich, M. Rudert and E. Willbold, *Journal of Biomedical Materials Research Part A*, 2007, 81A, 748-756.
2. M. P. Staiger, A. M. Pietak, J. Huadmai and G. Dias, *Biomaterials*, 2006, 27, 1728-1734.
3. M. Niinomi and M. Nakai, *INT. J. Biomater*, 2011, 2011, 10.
4. C. E. Wen, M. Mabuchi, Y. Yamada, K. Shimojima, Y. Chino and T. Asahina, *Scripta Mater.*, 2001, 45, 1147-1153.
5. F. Zhu, J. Wang, S. Li and J. Zhang, *Appl. Surf. Sci.*, 2012, 258, 8985-8990.
6. F. Witte, J. Fischer, J. Nellesen, H.-A. Crostack, V. Kaese, A. Pisch, F. Beckmann and H. Windhagen, *Biomaterials*, 2006, 27, 1013-1018.
7. Y. M. Wang, F. H. Wang, M. J. Xu, B. Zhao, L. X. Guo and J. H. Ouyang, *Appl. Surf. Sci.*, 2009, 255, 9124-9131.
8. N. I. Zainal Abidin, D. Martin and A. Atrens, *Corros. Sci.*, 2011, 53, 862-872.
9. N. I. Zainal Abidin, A. D. Atrens, D. Martin and A. Atrens, *Corros. Sci.*, 2011, 53, 3542-3556.
10. Y. C. Li, C. S. Wong, C. Wen and P. D. Hodgson, *Mater Technol*, 2012, 27, 49-51.
11. Y.-L. Zhou, Y. Li, D.-M. Luo, C. Wen and P. Hodgson, *J Mater Sci*, 2012, 48, 1632-1639.
12. N. Erdmann, N. Angrisani, J. Reifenrath, A. Lucas, F. Thorey, D. Bormann and A. Meyer-Lindenberg, *Acta Biomater.*, 2011, 7, 1421-1428.
13. Z. Li, X. Gu, S. Lou and Y. Zheng, *Biomaterials*, 2008, 29, 1329-1344.
14. L. Xu, G. Yu, E. Zhang, F. Pan and K. Yang, *Journal of Biomedical Materials Research Part A*, 2007, 83A, 703-711.
15. I. Stulikova and B. Smola, *Mater. Charact.*, 2010, 61, 952-958.
16. E. Zhang, D. Yin, L. Xu, L. Yang and K. Yang, *Materials Science and Engineering: C*, 2009, 29, 987-993.
17. X. Gu, Y. Zheng, Y. Cheng, S. Zhong and T. Xi, *Biomaterials*, 2009, 30, 484-498.
18. S. Zhang, X. Zhang, C. Zhao, J. Li, Y. Song, C. Xie, H. Tao, Y. Zhang, Y. He, Y. Jiang and Y. Bian, *Acta Biomater.*, 2010, 6, 626-640.

19. A. C. Hänzi, I. Gerber, M. Schinhammer, J. F. Löffler and P. J. Uggowitzer, *Acta Biomater.*, 2010, 6, 1824-1833.
20. D. Krewski, R. A. Yokel, E. Nieboer, D. Borchelt, J. Cohen, J. Harry, S. Kacew, J. Lindsay, A. M. Mahfouz and V. Rondeau, *Journal of Toxicology and Environmental Health, Part B*, 2007, 10, 1-269.
21. J. R. Walton, *J. Alzheimer's Dis.*, 2013, 35, 7-43.
22. Y. Li, M. Li, W. Hu, P. Hodgson and C. Wen, *Mater. Sci. Forum*, 2010, 654 - 656, 2192 - 2196.
23. N. T. Kirkland, J. Lespagnol, N. Birbilis and M. P. Staiger, *Corros. Sci.*, 2010, 52, 287-291.
24. K. M. Erikson, T. Syversen, J. L. Aschner and M. Aschner, *Environ. Toxicol. Pharmacol.*, 2005, 19, 415-421.
25. D. Ding, J. Roth and R. Salvi, *Neurotoxicology*, 2011, 32, 233-241.
26. N. A. Bock, F. F. Paiva, G. C. Nascimento, J. D. Newman and A. C. Silva, *Brain Res.*, 2008, 1198, 160-170.
27. J. Brandão-Neto, V. Stefan, B. B. Mendonça, W. Bloise and A. V. B. Castro, *Nutrition Research*, 1995, 15, 335-358.
28. G. J. Fosmire, *The American journal of clinical nutrition*, 1990, 51, 225-227.
29. M. D. Lastra, R. Pastelin, A. Camacho, B. Monroy and A. E. Aguilar, *J. Trace Elem. Med Biol.*, 2001, 15, 5-10.
30. E. Weigand and C. Boesch-Saadatmandi, *Lipids*, 2012, 47, 291-302.
31. F. E. Gürsel, A. Ateş, T. Bilal and A. Altiner, *Biol. Trace Elem. Res.*, 2012, 148, 378-382.
32. J. I. Post, J. K. Eibl and G. M. Ross, *Amyotrophic Lat. Scler.*, 2008, 9, 149-155.
33. Y. C. Lee, A. K. Dahle and D. H. StJohn, *Metall and Mat Trans A*, 2000, 31, 2895-2906.
34. K. W. Guo, *Recent Patents on Corrosion Science*, 2010, 2, 13-21.
35. M. Roy, G. Fielding and S. Bose, *Ceram. Trans.*, 2012, 237, 227-237.
36. E. Landi, J. Uggeri, V. Medri and S. Guizzardi, *Journal of Biomedical Materials Research Part A*, 2013, 101, 2481-2490.
37. M. Bornapour, M. Celikin and M. Pekguleryuz, *Materials Science and Engineering: C*, 2015, 46, 16-24.

38. Y. Li, C. Wen, D. Mushahary, R. Sravanthi, N. Harishankar, G. Pande and P. Hodgson, *Acta Biomater.*, 2012, 8, 3177-3188.
39. Y. Ding, C. Wen, P. Hodgson and Y. Li, *Journal of Materials Chemistry B*, 2014, 2, 1912-1933.
40. S. Guangling, *Corros. Sci.*, 2007, 49, 1696-1701.
41. Z. Shi, M. Liu and A. Atrens, *Corros. Sci.*, 2010, 52, 579-588.
42. G. Song, A. Atrens and D. St John, 2001.
43. M. C. Zhao, M. Liu, G. L. Song and A. Atrens, *Adv. Eng. Mater.*, 2008, 10, 104-111.
44. X. N. Gu, X. H. Xie, N. Li, Y. F. Zheng and L. Qin, *Acta Biomater.*, 2012, 8, 2360-2374.
45. Y. Song, E.-H. Han, D. Shan, C. D. Yim and B. S. You, *Corros. Sci.*, 2012, 65, 322-330.
46. G. L. Song and A. Atrens, *Adv. Eng. Mater.*, 1999, 1, 11-33.
47. G. Song, A. Atrens, D. S. John, X. Wu and J. Nairn, *Corros. Sci.*, 1997, 39, 1981-2004.
48. F. Cao, Z. Shi, G.-L. Song, M. Liu and A. Atrens, *Corros. Sci.*, 2013, 76, 60-97.
49. M. M. Avedesian and H. Baker, in *Magnesium and Magnesium alloys*, ed. M. Avedesian and H. Baker, ASM Int., Materials Park, 2<sup>nd</sup> edn, 1999, pp. 13-19.
50. H. Okamoto, *J Phase Equilib Diff*, 2007, 28, 305-306.
51. Y.-L. Zhou, Y. Li, D.-M. Luo, C. Wen and P. Hodgson, *J Mater Sci*, 2013, 48, 1632-1639.
52. G. Song, *Adv. Eng. Mater.*, 2005, 7, 563-586.
53. G. Ben-Hamu, D. Eliezer, K. S. Shin and S. Cohen, *J. Alloys Compd.*, 2007, 431, 269-276.
54. M. Bornapour, N. Muja, D. Shum-Tim, M. Cerruti and M. Pekguleryuz, *Acta Biomater.*, 2013, 9, 5319-5330.
55. Y. Zhu, G. Wu, Y.-H. Zhang and Q. Zhao, *Appl. Surf. Sci.*, 2011, 257, 6129-6137.
56. H. S. Brar, J. Wong and M. V. Manuel, *J. Mech. Behav. Biomed*, 2012, 7, 87-95.

57. B. A. Shaw, in *ASM Handbook* vol. 13 (A): *Fundamentals, Testing, and Protection*, ed. Lawrence J. Korb. and David L. Olson, ASM Int., Materials Park, 9<sup>th</sup> edn, 2003 , p. 695.
58. N. D. Nam, W. C. Kim, J. G. Kim, K. S. Shin and H. C. Jung, *J. Alloys Compd.*, 2011, 509, 4839-4847.
59. R. Lindström, L.-G. Johansson, G. E. Thompson, P. Skeldon and J.-E. Svensson, *Corros. Sci.*, 2004, 46, 1141-1158.
60. R. Iffland, in: *Handbook on Metals in Clinical and Analytical Chemistry: Arsenic*, ed. Hans Seiler, Astrid Sigel and Lelmut Sigel, Marcel Dekker Inc., New York, 1994, p. 238-252.
61. H. A. Schroeder, M. Mitchener, J. J. Balassa, M. Kanisawa and A. P. Nason, *The Journal Of Nutrition*, 1968, 95, 95-101.
62. L. Yang, Y. Huang, F. Feyerabend, R. Willumeit, C. Mendis, K. U. Kainer and N. Hort, *Acta Biomater.*, 2013, 9, 8499-8508.
63. D. Hong, P. Saha, D.-T. Chou, B. Lee, B. E. Collins, Z. Tan, Z. Dong and P. N. Kumta, *Acta Biomater.*, 2013, 9, 8534-8547.
64. W. Zhang, M. Li, Q. Chen, W. Hu, W. Zhang and W. Xin, *Materials & Design*, 2012, 39, 379-383.
65. D.-T. Chou, D. Hong, P. Saha, J. Ferrero, B. Lee, Z. Tan, Z. Dong and P. N. Kumta, *Acta Biomater.*, 2013, 9, 8518-8533.
66. X. N. Gu, N. Li, Y. F. Zheng and L. Ruan, *Materials Science and Engineering: B*, 2011, 176, 1778-1784.
67. Z. G. Huan, M. A. Leeflang, J. Zhou, L. E. Fratila-Apachitei and J. Duszczyk, *J. Mater. Sci. Mater. Med.*, 2010, 21, 2623-2635.
68. G. D. Clayton, . F. E. Clayton, *Occup Environ Med.*, 1996, 53, 359-360.
69. D. Mushahary, C. Wen, J. M. Kumar, J. Lin, N. Harishankar, P. Hodgson, G. Pande and Y. Li, *Colloids Surf. B. Biointerfaces*, 2014, 122, 719-728.
70. P. J. Marie, *Curr. Opin. Pharm.*, 2005, 5, 633-636.
71. P. J. Marie and M. Hott, *Metabolism*, 1986, 35, 547-551.
72. G. I. H. K. E. N. Tanaka, *Health Phys.*, 1981, 40, 601-614.
73. S. Pors Nielsen, *Bone*, 2004, 35, 583-588.
74. D. Olehy, R. Schmitt and W. Bethard, *J. Nucl. Med.*, 1966, 7, 917-927.
75. G. Manivasagam, D. Dhinasekaran and A. Rajamanickam, *Recent patents on corrosion science*, 2010, 2, 40-54.

76. X. N. Gu, Y. F. Zheng and L. J. Chen, *Biomed. Mater.*, 2009, 4, 1-8.
77. S. Virtanen, *Materials Science and Engineering: B*, 2011, 176, 1600-1608.
78. G. Song, A. Atrens, X. Wu and B. Zhang, *Corros. Sci.*, 1998, 40, 1769-1791.
79. L. Jonášová, F. A. Müller, A. Helebrant, J. Strnad and P. Greil, *Biomaterials*, 2004, 25, 1187-1194.



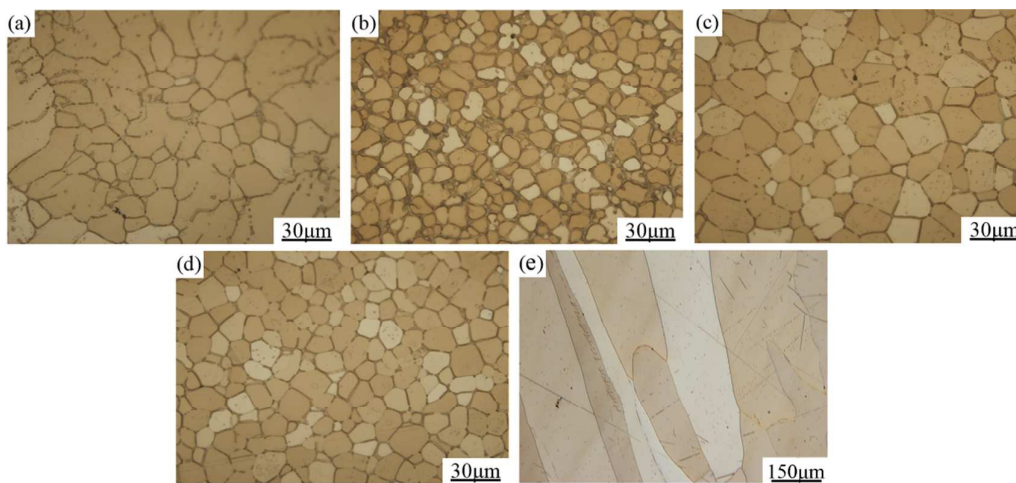


Fig. 1. Microstructures of Mg-Zr-Sr alloys: (a) Mg1Zr2Sr; (b) Mg1Zr5Sr; (c) Mg2Zr2Sr; (d) Mg5Zr2Sr; and (e) as-cast Mg.

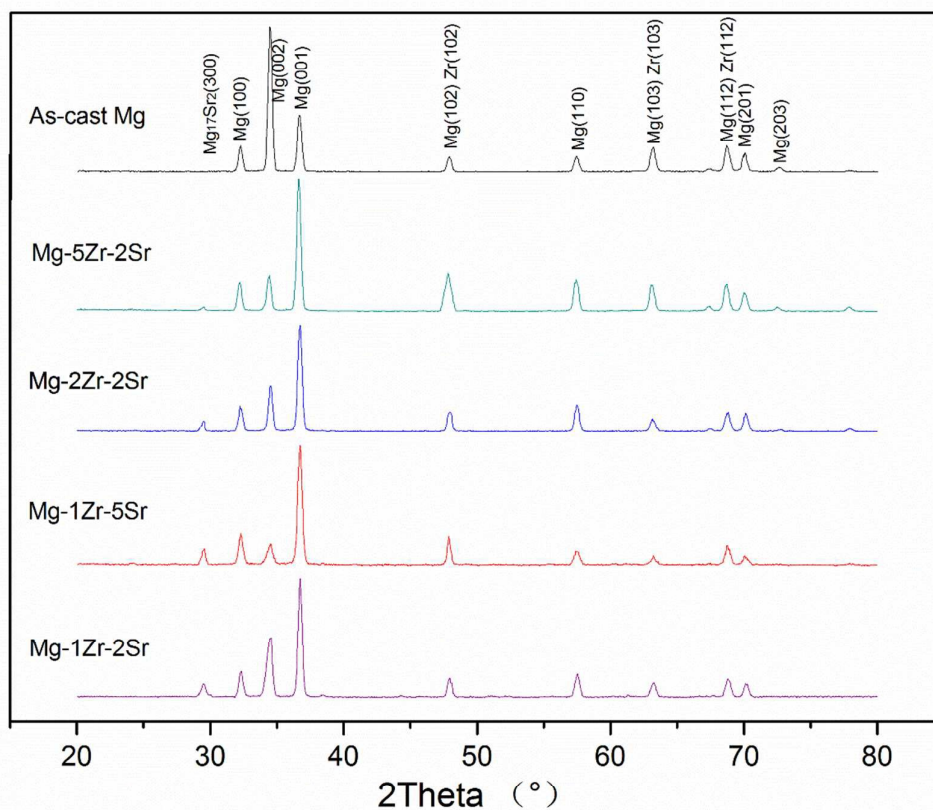
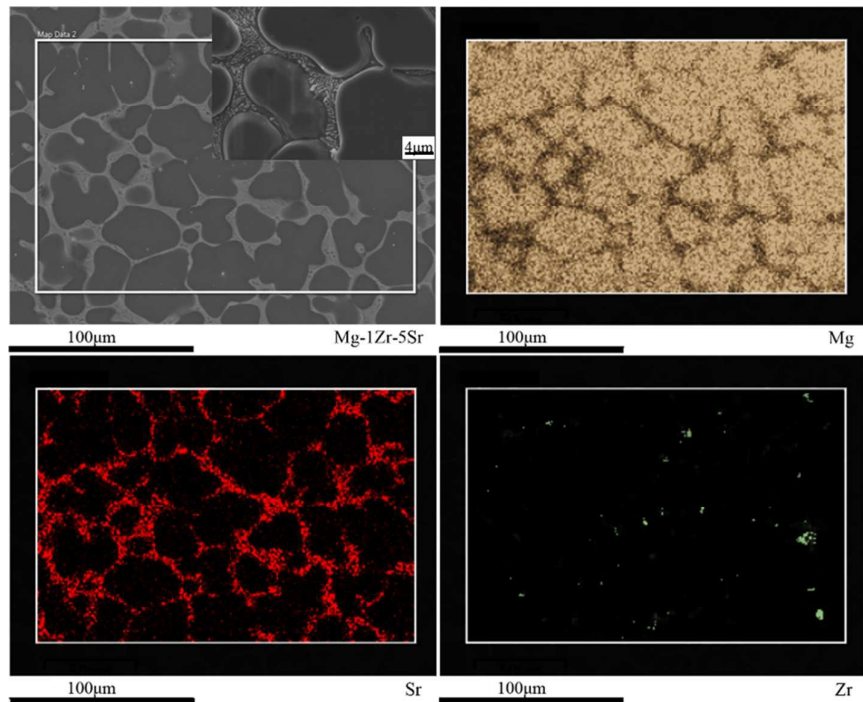
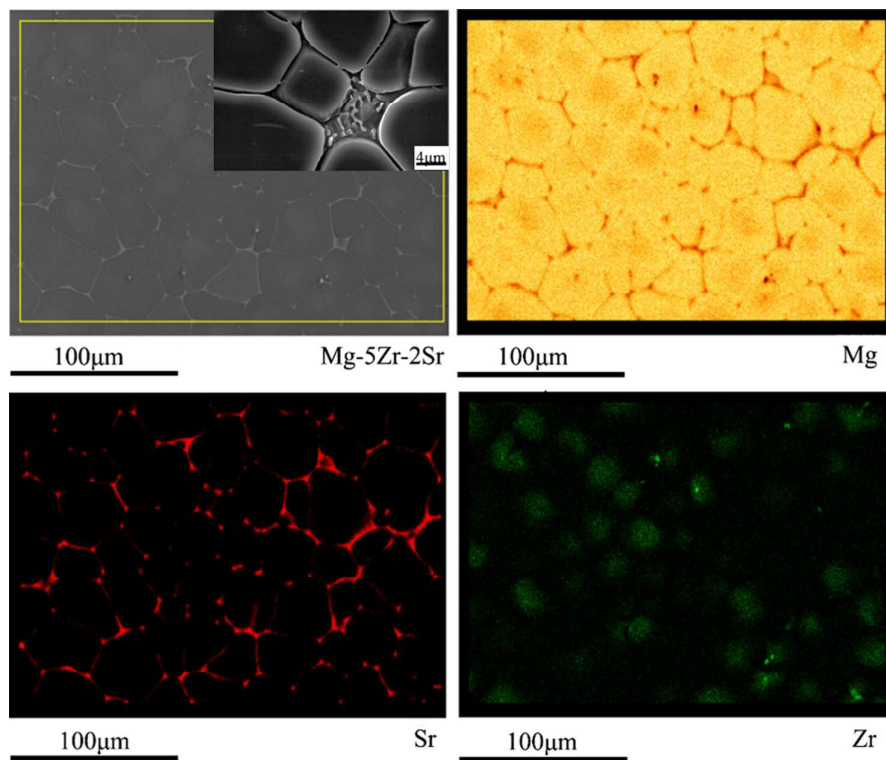


Fig. 2. XRD patterns of Mg-Zr-Sr alloys before immersion tests.

Fig. 3. EDX mapping of alloying elements for Mg<sub>1</sub>Zr<sub>5</sub>Sr.Fig. 4. EDX mapping of alloying elements for Mg<sub>5</sub>Zr<sub>2</sub>Sr.

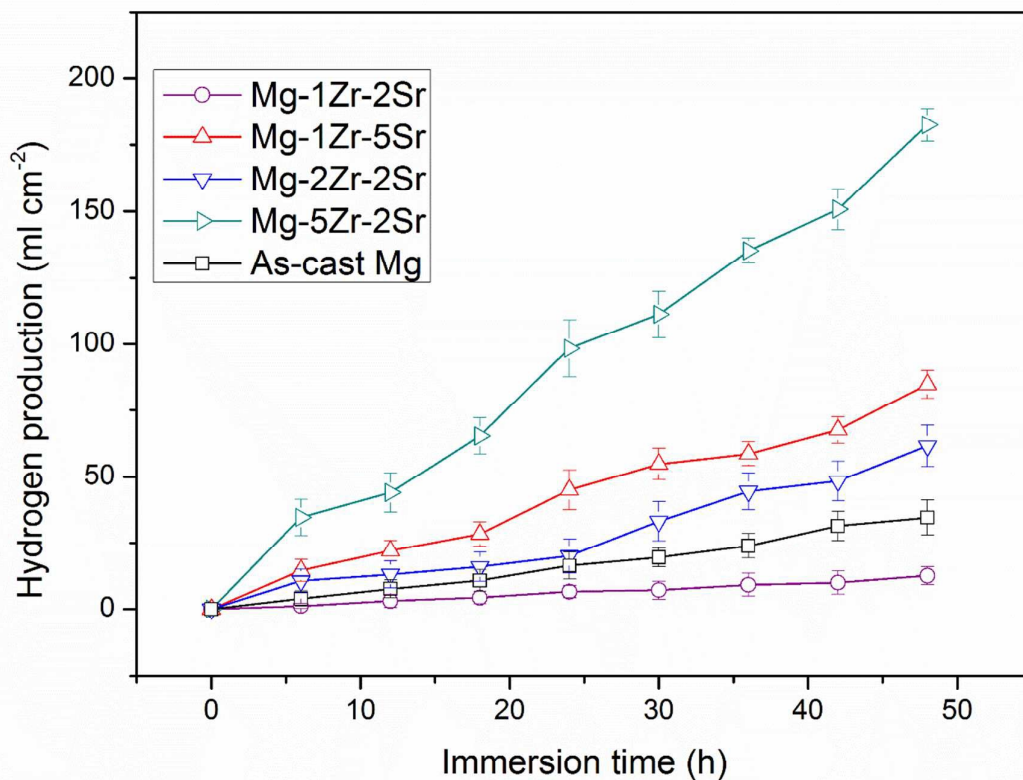


Fig. 5. Hydrogen evolution of Mg-Zr-Sr alloys immersed in SBF.

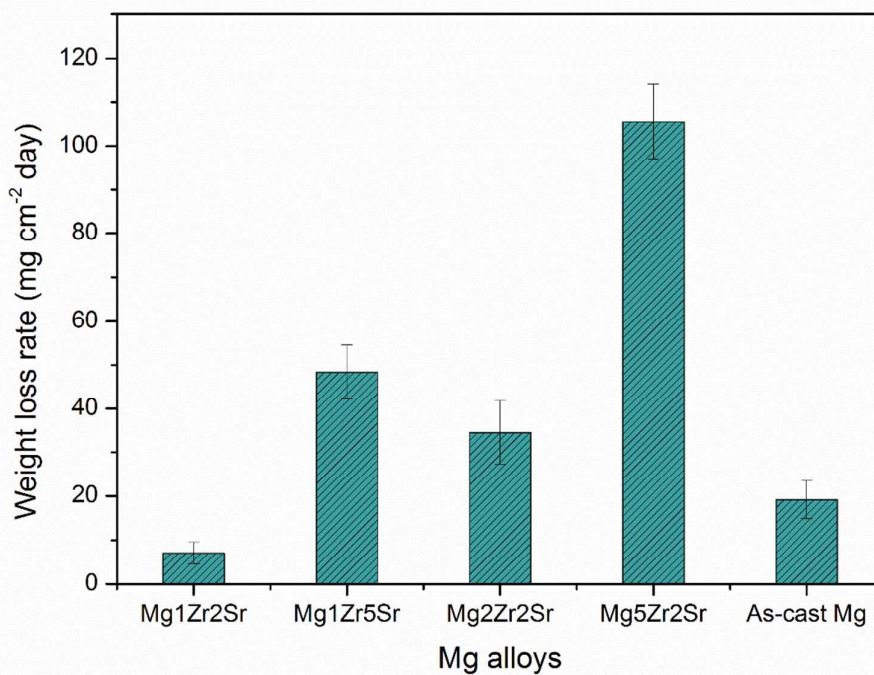


Fig. 6. Weight loss rates of Mg alloys in SBF.

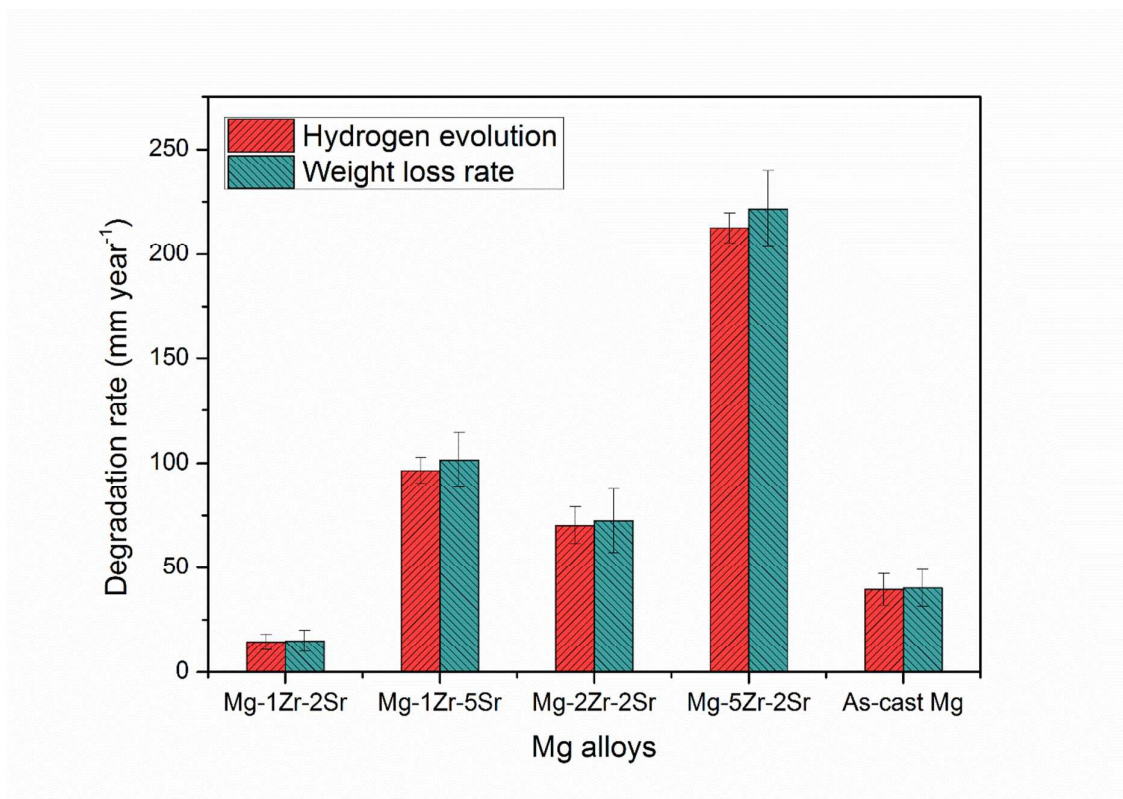


Fig. 7. Degradation rates of Mg-Zr-Sr alloys and as-cast Mg reference.

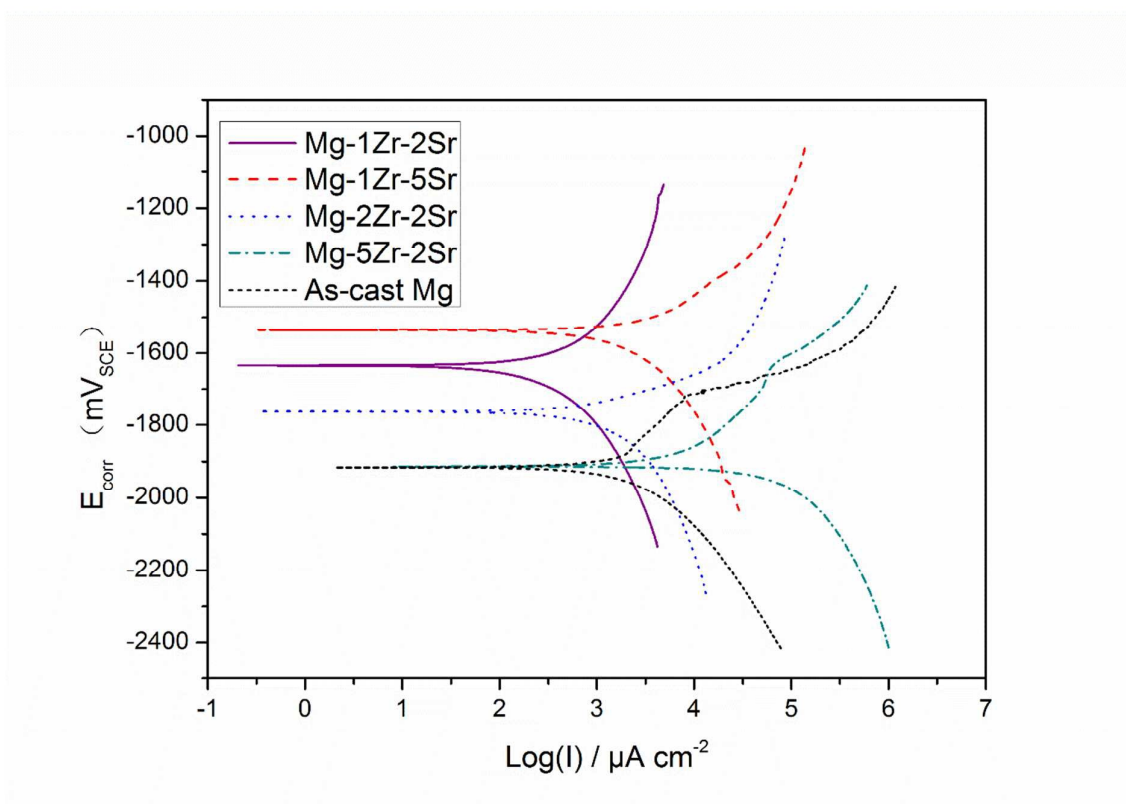
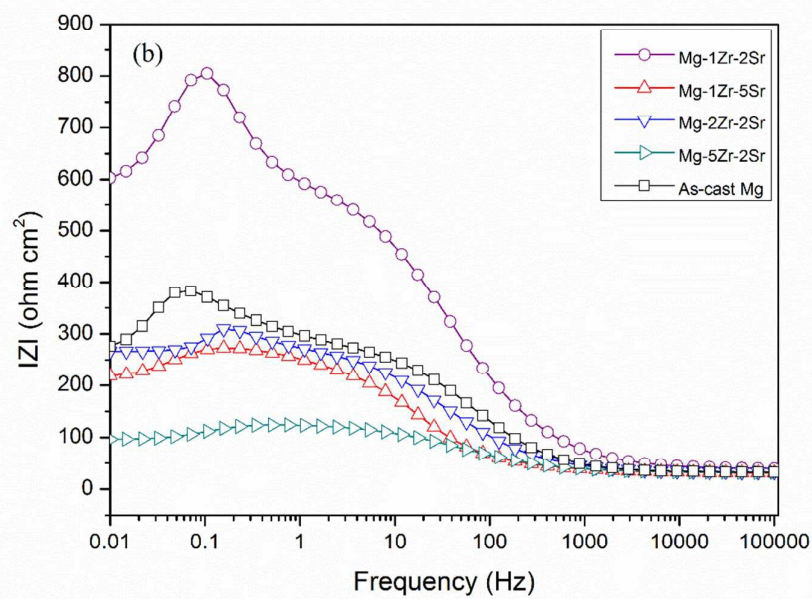
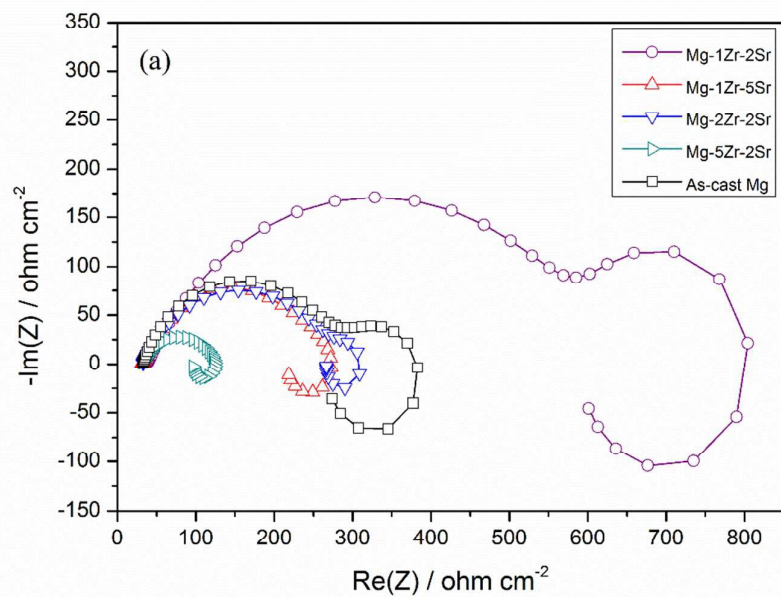


Fig. 8. Polarization curves of Mg-Zr-Sr alloys after 2 h immersion in SBF.



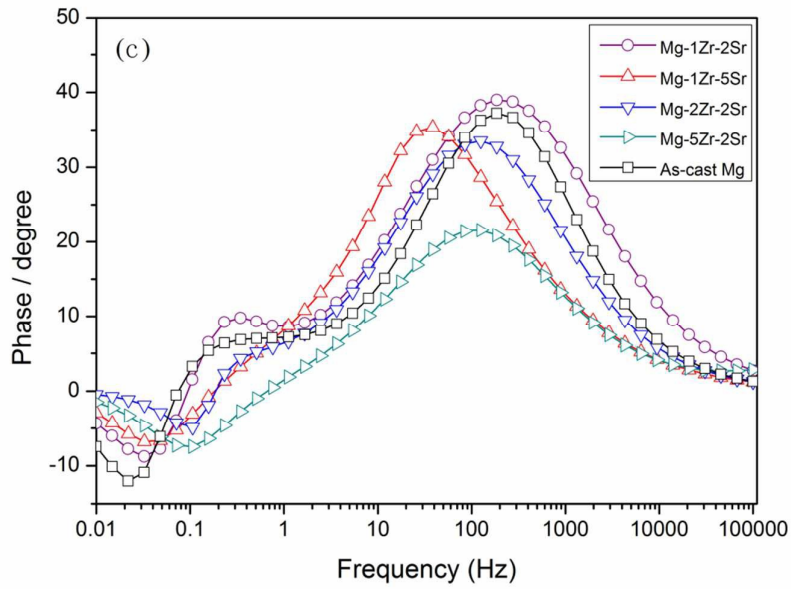


Fig. 9. EIS spectra of Mg-Zr-Sr alloys after 2 h stabilization in SBF: (a) Nyquist plots; (b) Bode plots of  $|Z|$  vs. frequency; and (c) Bode plots of phase vs. frequency.

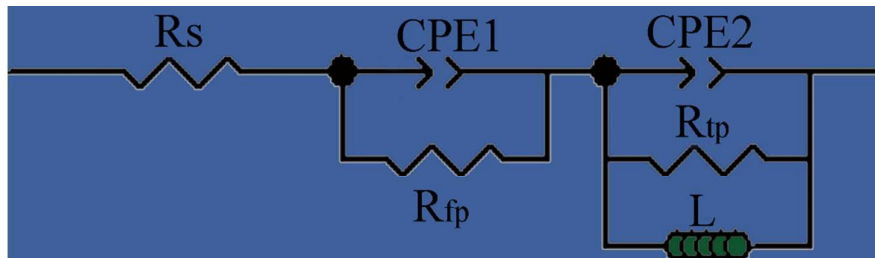


Fig. 10. Equivalent circuits of the EIS spectra.

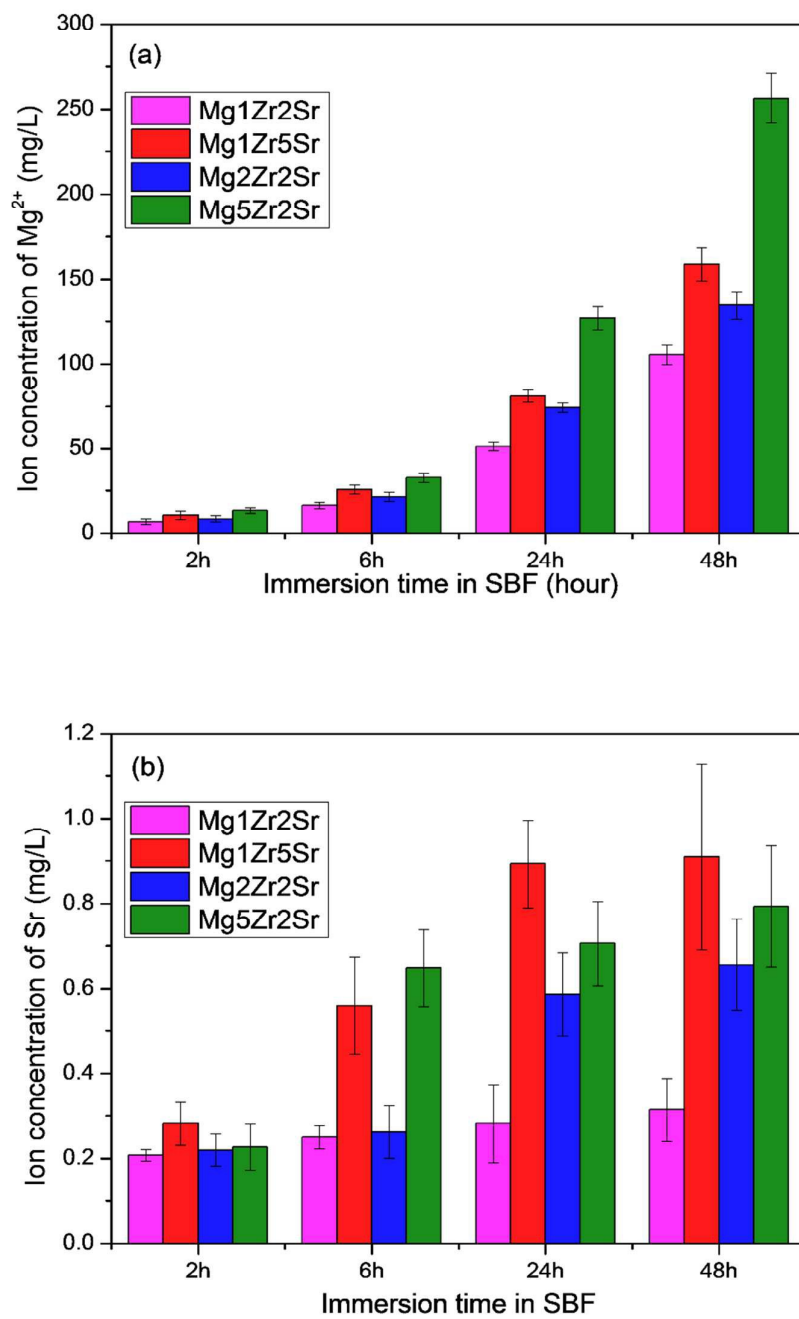


Fig. 11 Variations of (a) Mg and (b) Sr ion concentrations in SBF

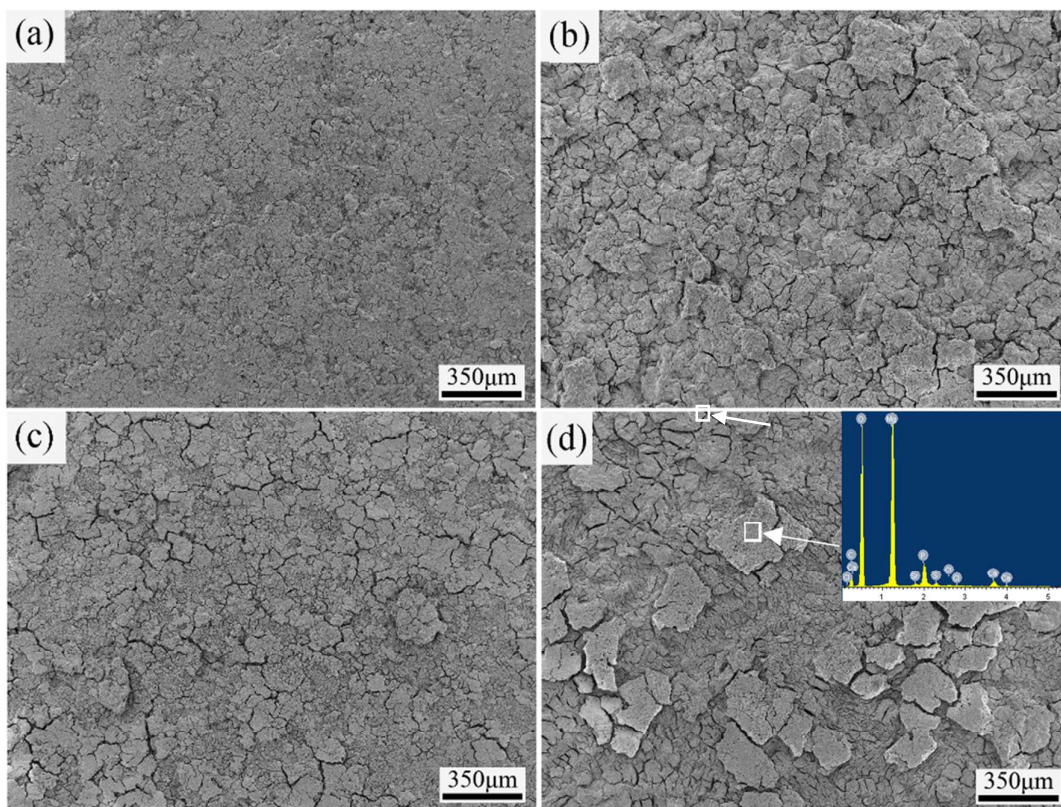


Fig. 12. Degradation morphologies of Mg-Zr-Sr alloys after polarization tests in SBF: (a) Mg<sub>1</sub>Zr<sub>2</sub>Sr; (b) Mg<sub>1</sub>Zr<sub>5</sub>Sr; (c) Mg<sub>2</sub>Zr<sub>2</sub>Sr; and (d) Mg<sub>5</sub>Zr<sub>2</sub>Sr.

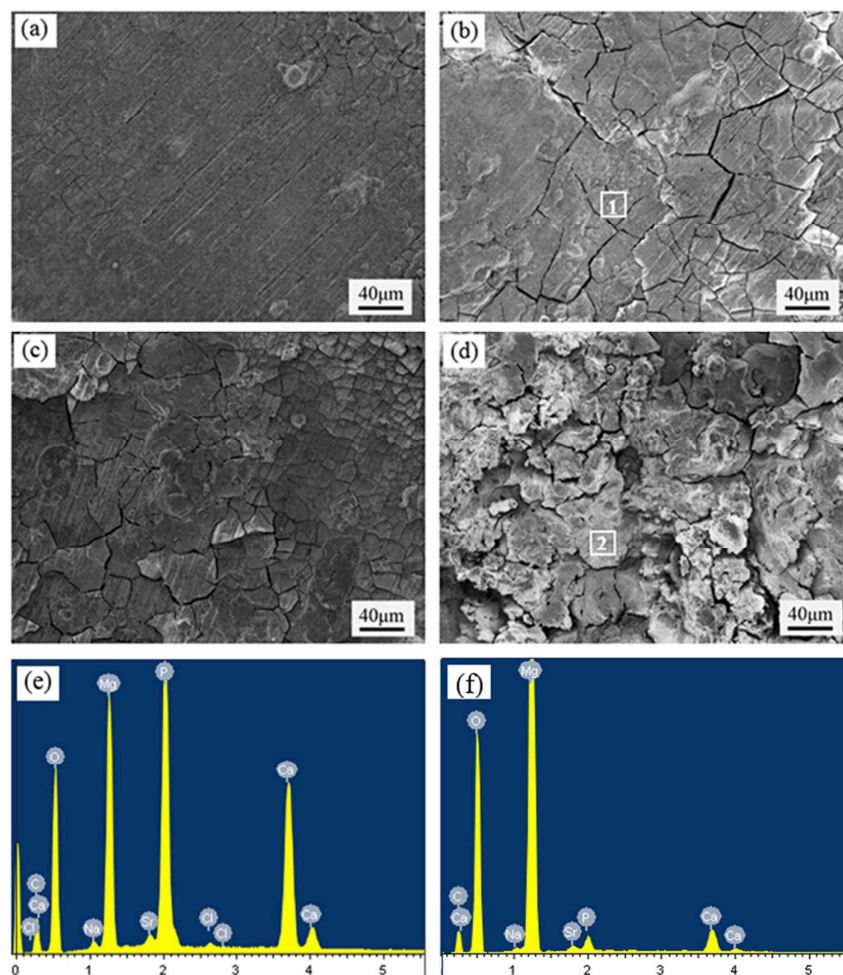


Fig. 13. Surface morphologies of Mg-Zr-Sr alloys after immersion in SBF for 6 h: (a) Mg1Zr2Sr; (b) Mg1Zr5Sr; (c) Mg2Zr2Sr; (d) Mg5Zr2Sr; and (e) EDX of spot 1 on the surface of Mg1Zr5Sr; and (f) EDX of spot 2 on the surface of Mg5Zr2Sr.

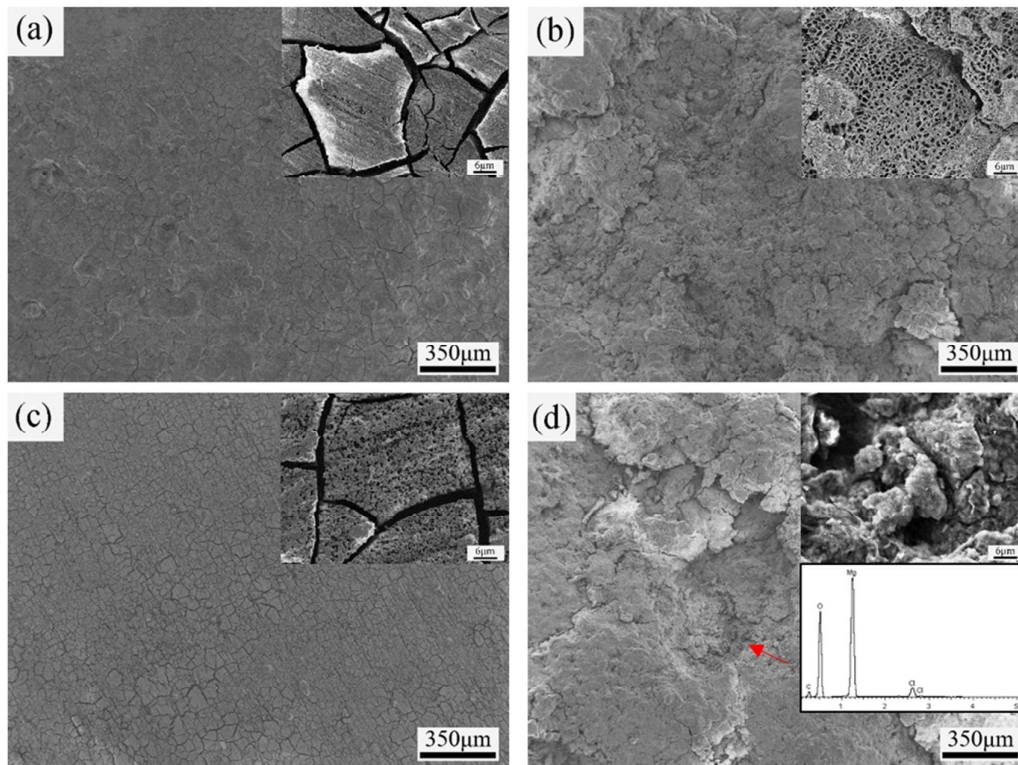


Fig. 14. Surface morphologies of Mg-Zr-Sr alloys after immersion in SBF for 24 h: (a) Mg1Zr2Sr; (b) Mg1Zr5Sr; (c) Mg2Zr2Sr; and (d) Mg5Zr2Sr.

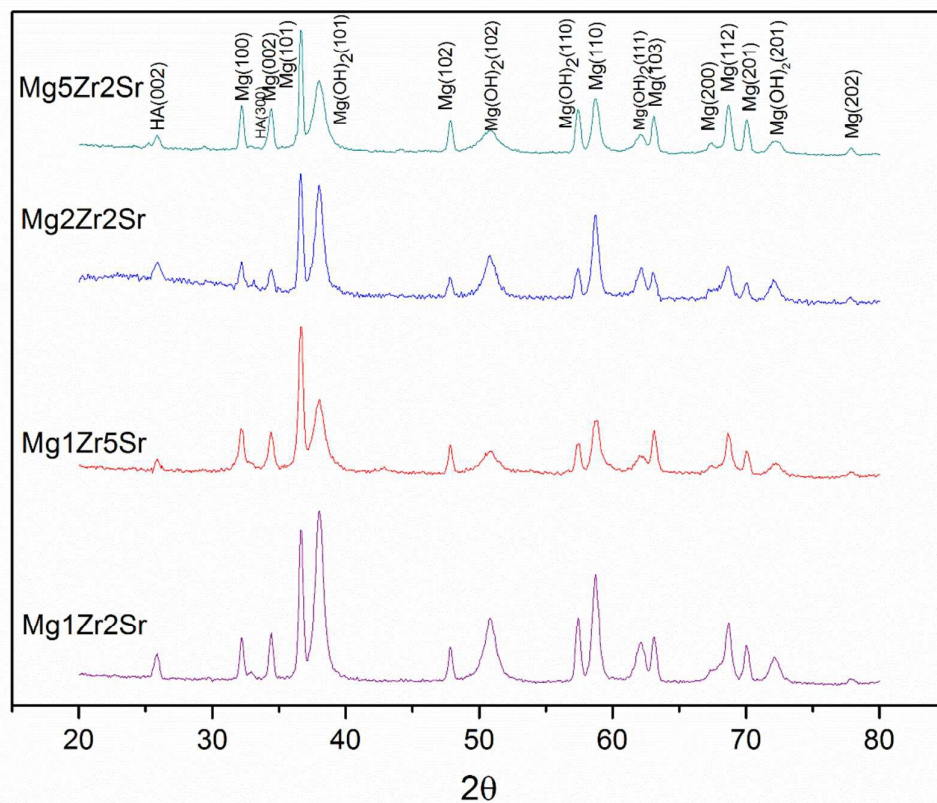


Fig. 15. XRD patterns of Mg-Zr-Sr alloys after 24 h immersion in SBF.

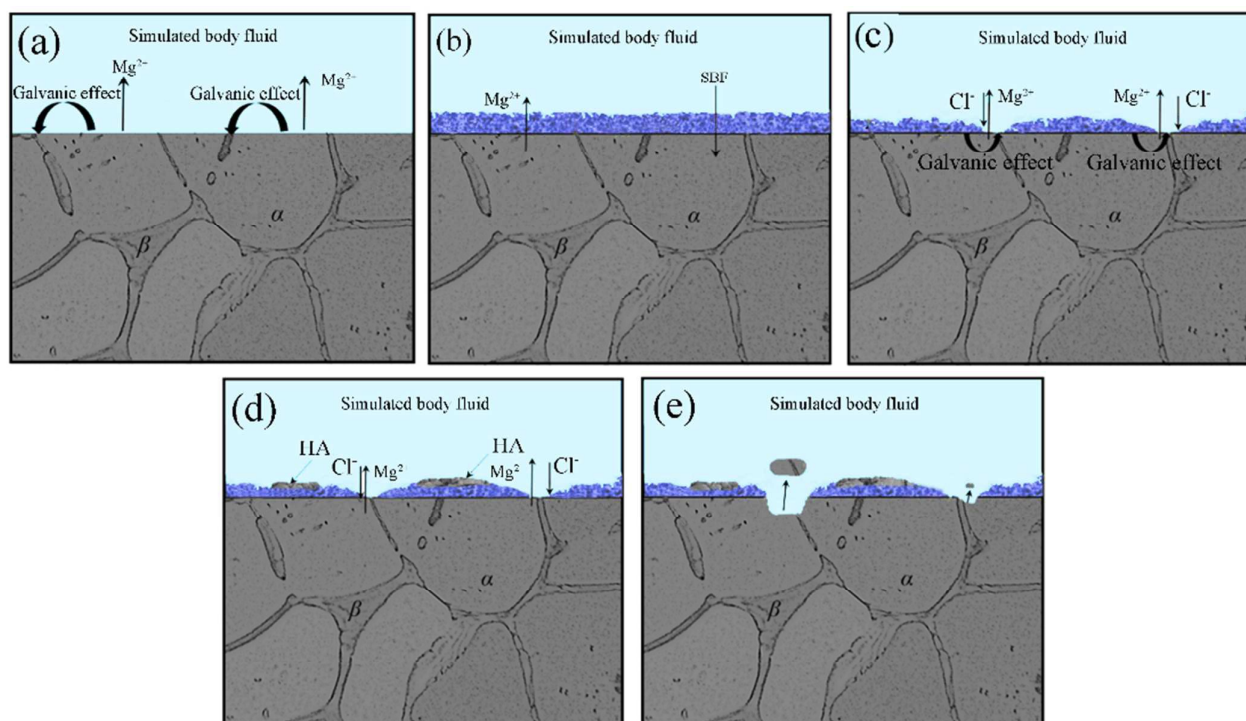


Fig. 16. Schematic model for biocorrosion propagation of Mg-Zr-Sr alloys in SBF: (a) dissolution of Mg matrix due to galvanic effects; (b) partially protective film of  $Mg(OH)_2$ ; (c) dissolution of  $Mg(OH)_2$  due to deterioration by  $Cl^-$ ; (d) formation of HA; (e) corrosive residues escaping from Mg matrix.

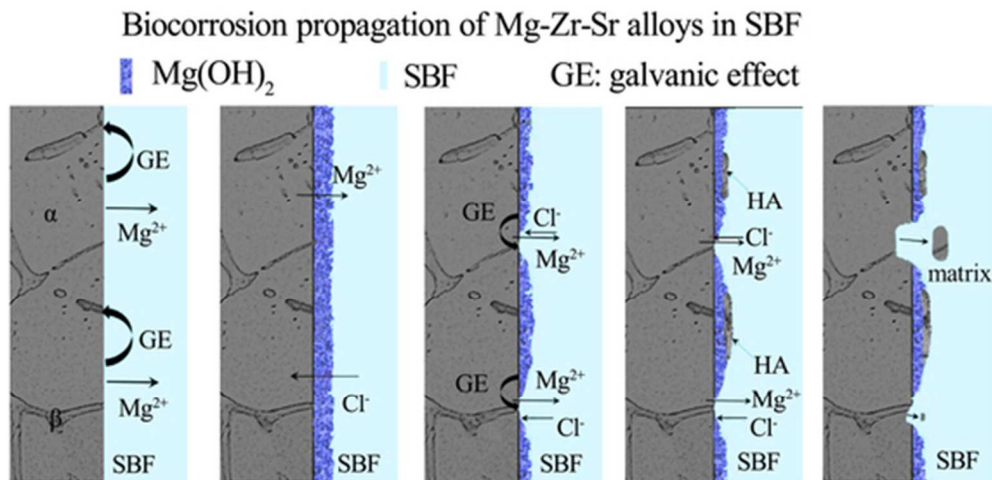
Table 1. Corrosion of Mg-Zr-Sr alloys and as-cast Mg in SBF

Materials	Hydrogen evolution rate (ml cm <sup>-2</sup> day <sup>-1</sup> )	Corrosion rate* (mm year <sup>-1</sup> )	Weight loss rate (mg cm <sup>-2</sup> day <sup>-1</sup> )	Corrosion rate** (mm year <sup>-1</sup> )	$i_{corr}$ (μA cm <sup>-2</sup> )	$P_i$ (mm y <sup>-1</sup> )***
Mg1Zr2Sr	6.31	14.39	7.05	14.80	499.62	11.42
Mg1Zr5Sr	42.36	96.53	48.32	101.47	3020.52	68.55
Mg2Zr2Sr	30.82	70.23	34.5	72.45	2500.41	57.13
Mg5Zr2Sr	93.31	212.64	105.51	221.58	6714.33	153.09
As-cast Mg	17.32	39.47	19.13	40.18	1411.15	31.99

\* calculated on the H<sub>2</sub> evolution rate; \*\* calculated on the weight loss rate; \*\*\* calculated on the potentiodynamic polarization

Table 2. Fitting results of the EIS spectra

Specimen	$R_s$ ( $\Omega \text{ cm}^2$ )	$R_p$ ( $\Omega \text{ cm}^2$ )	$C_{1,T}$ ( $10^{-6} \text{ F cm}^{-2}$ )	$n_1$	$C_{2,T}$ ( $10^{-6} \text{ F cm}^{-2}$ )	$n_2$	$R_p$ ( $\Omega \text{ cm}^2$ )	$L$ ( $\text{H cm}^{-2}$ )
Mg-1Zr-2Sr	38.4	552.8	2104.4	1	53.9	0.6789	569.8	1402
Mg-1Zr-5Sr	30.4	188.9	783.8	0.5486	136.5	0.9857	78.1	258.9
Mg-2Zr-2Sr	32.3	224.6	115.5	0.7052	22.1	0.4524	115.7	47.93
Mg-5Zr-2Sr	31.2	96.2	270.9	0.6649	99.5	0.5495	32.13	46.4
As-cast Mg	32.1	238.9	52.1	0.7692	72.2	0.5218	192.3	584.5



48x23mm (300 x 300 DPI)